ELSEVIER

Eur. J. Mech. B/Fluids 21 (2002) 1–28

EUROPEAN JOURNAL OF MECHANICS B/FLUIDS

The coupling between turbulent, penetrative convection and internal waves

M.E. Michaelian [1], T. Maxworthy, L.G. Redekopp *

Department of Aerospace and Mechanical Engineering, University of Southern California, Los Angeles, CA 90089-1191, USA

Received 20 November 2000; received in revised form 15 May 2001; accepted 1 August 2001

Abstract

Experiments aimed at exploring the coupling of penetrative convection with internal waves in the adjoining, stable layer were performed in a long convection cell. The experiments are motivated by preliminary theoretical results suggesting that an intrinsic phase instability may exist in the coupled system in which case long internal waves modulate the height and strength of convective plumes. Using a temperature-controlled, stably stratified experimental apparatus, measured temperature data reveal the presence of long internal wave modes that persist for many convective time scales. The frequencies of these waves increase linearly in time during the energy transfer between the convective and stratified regions as the depth of the stratified region diminishes and the depth of the mixed layer increases. Temporal variations in the heat flux, interface rise characteristics, and frequencies of internal wave motions are reported. A natural temporal modulation of the thickness of the transition layer separating the mixed layer from the stratified layer occurs following commencement of heating, with the amplitude and frequency of the modulation varying with the initial stratification. Temperature variance data suggest that a fairly strong interaction between convection and internal waves occurs, especially when the interface region is midway between the upper and lower boundaries of the cell and the no-slip boundary conditions play a less influential role on the dynamics of the coupling.

Keywords: Penetrative convection; Internal waves

1. Introduction

Convection in response to surface heating in the atmosphere or surface cooling in the ocean occurs in a finite layer bounded on one side by a stably-stratified layer. In each case convective motions penetrate into the contiguous stratified layer and force dynamic deformations of isopycnal surfaces. The scale of these deformations extends from the scale of individual convective plumes to long-wave modulations of the convecting layer. Although the characteristic time scale for convective motion is relatively slow, the spectrum of propagating internal waves includes long waves of vanishing frequency. Consequently, it is not unreasonable to expect a relatively strong coupling to exist between convective motions in a mixed layer with internal waves in an adjoining layer, especially with long internal waves. The questions of practical concern relative to this possible coupling pertain to the rate of energy transfer from convective motions to internal waves; the extent to which internal waves can affect convective motions within, and the heat flux across, the mixed layer; and the principle mechanism(s) through which this coupling is realized.

* Correspondence and reprints.
E-mail addresses: Mark.Michaelian@trw.com (M.E. Michaelian), maxworth@usc.edu (T. Maxworthy), redekopp@spock.usc.edu (L.G. Redekopp).
[1] Present address: TRW Space and Technology Division, Space & Electronics Group, One Space Park, R1/1028B, Redondo Beach, CA 90278, USA

0997-7546/02/$ – see front matter
PII: S0997-7546(01)01158-X

To clarify further some of the issues pertaining to the nature and strength of the possible coupling between convection in a mixed layer and internal waves in adjoining layers, consider the specific case of surface cooling of the upper mixed layer in a lake or ocean containing a weak, (approximately) 'interfacial' thermocline. To a first approximation the air-sea interface is non-deformable, at least so far as convective motions are concerned, due to the strong density discontinuity across the interface ($\Delta\rho/\rho \sim \mathcal{O}(10^3)$). By comparison, the density change across the 'interface' at the base of the mixed layer is indeed small ($\Delta\rho/\rho \sim \mathcal{O}(10^{-2})$ or smaller) and the boundary between the contiguous layers can be deformed quite readily, even by the relatively weak motions occurring in convective cells or plumes. In addition, the air-sea boundary is essentially stress-free in so far as the leading-order convective motions are concerned. This latter point is of fundamental significance relative to the coupling between convection and internal waves in that the dynamical system is, therefore, Galilean invariant and long internal waves can readily advect the convective structures. The breaking of the Galilean invariance by the appearance of an internal wave then suggests the possible existence of an unstable phase mode arising from the coupling between the convective structures and the horizontal velocity field associated with long (i.e., low frequency) internal waves (cf. Coullet and Huerre [1]; Bernoff [2]; Newell et al. [3]). Furthermore, the weak density 'interface' at the base of the mixed layer is susceptible to vertical deformation, associated in particular with a long internal wave, releasing a large-scale horizontal pressure-gradient field. The confluence of these effects suggests a rich, intrinsic coupling between the two classes of motion, convection and internal waves.

A dynamical model of the flow situation just described, and one that illuminates the inherent coupling mechanisms, was developed by Pavithran and Redekopp [4]. They derived a set of evolution equations describing the coupled convection-internal wave fields for a two-dimensional, infinite aspect ratio configuration under the restriction that the Rayleigh number was near the critical value for the onset of convection. The model and some of its implications are reviewed briefly since they provide both the motivation and some relevant conceptual underpinnings for the present work.

Let $A(x,t)$ denote the slowly-varying complex amplitude of the vertical velocity field in space and time with fundamental wave number k_c (i.e., $w \sim A(x,t)\exp(ik_c x)$, with the subscript c denoting the critical condition at Rayleigh number Ra_c); let $U(x,t)$ represent the slowly-varying horizontal velocity field associated with the internal wave field and the breaking of the Galilean invariance of the base (undisturbed) state; and let $H(x,t)$ define the slowly-varying deformation of the 'interfacial' thermocline from its equilibrium position. Then, the evolution system for the coupled dynamics can be written in the following normalized form:

$$A_t + ik_c UA = \Delta A - rHA + A_{xx} - |A|^2 A + \text{h.o.t.}, \tag{1}$$

$$U_t + \beta H_x = \sigma\left(|A|^2\right)_x + \lambda U_{xx} + UU_x + \text{h.o.t.}, \tag{2}$$

$$H_t + U_x = \alpha H_{xx} - \nu\left(|A|^2\right)_{xx} + (UH)_x + \text{h.o.t.} \tag{3}$$

The criticality (or linear growth rate) parameter Δ is positive for Rayleigh numbers above Ra_c and negative for Rayleigh numbers below Ra_c. This evolution system can be postulated entirely on the basis of invariance principles, but was derived by means of a rational asymptotic approximation for a simple 'interfacial' thermocline model.

It is important to comment that there exists a forced 'short-wave' deformation of the thermocline associated with the convective motions occurring on the scale of the fundamental wave number k_c (interfacial displacement $\zeta \sim A\exp(ik_c x)$, say). The forced response induces internal wave motions possessing moderate frequencies and relatively high vertical wave number; that is, vertically propagating waves. This forced-radiated field represents an energy sink for convective motion, albeit a relatively weak, passive one. The strongest coupling, however, enters through the large-scale (i.e., long wave) coupling manifested by the slowly-varying fields $U(x,t)$ and $H(x,t)$. It was shown by Pavithran and Redekopp [4] that this coupling releases an intrinsic mode of instability which is principally associated with the phase of the complex amplitude function $A(x,t)$. The magnitude of the complex amplitude function, and hence the strength of the convecting field, is slaved to the phase. It is for this reason termed a phase instability.

An insight into the principle mechanism underlying the coupling under consideration here can be gleaned by an examination of the evolution system (equations (1)–(3)). First, the breaking of the translational invariance of the base state by the fundamental mode with wave number k_c is described by the system comprised of the terms in equation (1) involving only $A(x,t)$. The single PDE containing these terms alone is precisely the Newell–Whitehead–Segel equation (cf. Newell and Whitehead [5]; Segel [6]). This equation describes the spontaneous instability of a finite amplitude roll state termed the Eckhaus instability. This instability is intrinsic to any finite-amplitude array of convecting rolls with or without stress-free boundaries. It is a phase instability associated with the broken translational invariance of the system. Second, weak spatial inhomogeneities in the convection field (the $\sigma(|A|^2)_x$ term in equation (2)) stimulated by either external conditions or an intrinsic mode of instability drives a large-scale velocity field $U(x,t)$ which, in turn, affects the phase of the convection field via the Doppler-shift term $ik_c UA$ in equation (1). This action arises from the breaking of the Galilean invariance of the base state associated directly with the presence of stress-free boundaries as described by Coullet and Huerre [1]. For the nominal case of convection between fixed (i.e., non-deformable) stress-free surfaces, this state is only released at leading order when the modulation of the convection field is two-dimensional, the coupling being realized through a large-scale vertical vorticity field. It is significant to note that

the coupling between the $U(x,t)$ and the $A(x,t)$ fields can be realized in one-dimensional modulations of the convecting state at leading order when the restriction of non-deformable surfaces is relaxed, as in the present context. The third effect captured implicitly in the evolution system, that of wave propagation, is released by the coupling between the $U(x,t)$ field and the large-scale pressure gradient field represented by deformations $H(x,t)$ of the boundary between the mixed layer and the adjoining stratified region. It is immediately apparent that the left-hand sides of equations (2) and (3) define the linear wave equation in the shallow-water limit for the 'interfacial' thermocline model. The coupling between this mode and convection, represented by the term rHA in equation (1), corresponds to the modulation of the local super-criticality (Rayleigh number) as propagating or standing long waves cause the depth of the convecting layer to vary. Hence, an interacting convection-internal wave model emerges showing that the dominant coupling enters through the large-scale fields, an interaction that might be expected to be quite common in large aspect-ratio systems; that is, in natural environments. The combination of the three interactions discussed here, and described by the weakly nonlinear system (equations (1)–(3)), is an intrinsic, co-dimension-three dynamics whose consequence for convective transport in natural systems merits, we believe, further investigation.

The analytical model described above applies specifically to convection in a layer adjacent to a stress-free boundary. The presence of a no-slip boundary destroys the Galilean invariance of the system and severely weakens the possibility of coupling between convection and internal waves in an adjoining layer. Physically, the sloshing of the convective structures by a long internal wave will be impeded by the no-slip boundary. The coupling effect is still present, albeit considerably weaker in magnitude and occurring on a slower time scale. One may argue, however, that the stronger coupling may still be realized at high Rayleigh numbers in the presence of no-slip boundaries, especially at lower Prandtl numbers, when convective motions in the bulk of the mixed layer are somewhat shielded from the no-slip boundary condition though a thin boundary layer adjacent to this surface. That is, although the no-slip condition applies, convective plume structures can still be subjected to considerable modulation and tilting by a long internal wave, especially when these structures are tall and slender compared to the boundary layer thickness adjacent to the heated (or, cooled) boundary. Admittedly, these comments are speculative and await validation or rejection by means of a controlled physical or numerical experiment. The present study is offered as an attempt to clarify and quantify at least some of these effects.

The work presented here involves a laboratory experiment of penetrative convection into a stably-stratified fluid in a large aspect ratio cell. The convection cell is purposely designed to be long compared with its width so that a preferred orientation of the longest internal wave, and a clear separation in the lowest frequency of possible internal wave modes, is unambiguous. Furthermore, the depth of the cell is also small compared with its length so that a well-defined, ducted long wave exists. By the very nature of penetrative convection, however, the depth of the convecting layer changes continuously on a time scale commensurate with that for convective overturning. The varying depth implies a continuously-changing scale for the internal wave guide associated with the stably-stratified layer. The model represented by equations (1)–(3) specifically assumes that some unspecified large-scale processes maintain the depth of the mixed layer essentially constant on the scale of several long wave periods. The lack of separation of time scales in most contexts of penetrative convection is difficult to capture in any analytical model of the phenomena. This serves as another motivation for the physical experiment described below.

A number of previous studies have examined some of the characteristics of convective motion penetrating into a stably stratified layer. Townsend [7,8] examined specifically the case of excitation of internal waves by a layer of active convective motions adjacent to a stable layer. He noted that the rising convective motions were more columnar, or plume-like, than spherical thermals, and that these plume-like motions excited transient, propagating internal wave groups whose phase speeds were approximately equal to the excitation velocities in the plumes. He noted in particular that the group velocity of these packets was close to the horizontal, indicating the presence of low frequencies. Furthermore, he found that the largest fluctuations occurred near the bottom of the stratified layer. We note that this is a level where the internal wave eigenfunction of the lowest mode(s) for the associated wave guide is expected to be a maximum. Townsend noted also that the superposition of waves excited by the collective action of plumes having a wide band of energies and phases led to wave disturbances distributed over the entire depth of the stratified layer. This observation could be consistent with an internal wave field comprised of low-mode, long internal waves commensurate with the size of the cell, or by higher-frequency, vertically-propagating local waves, or both. No definitive characterization of the excited wave field was made, perhaps partly because of the relatively small aspect ratio of the cell so that a clear separation of the short and long wave motions could not be made.

In a study of penetrative convection in water, Deardorff et al. [9] noted that the frequency of temperature fluctuations in the convective layer was decidedly higher than those in the stratified layer. This observation points to the presence of low-frequency internal waves, but no discussion of the dominant horizontal wave lengths was provided. They also reported that the internal wave field appeared to increase in amplitude when the transition layer approached the temperature sensor in the stratified layer. This may imply that the strength of the wave field, as they suggest, decays away from the transition layer. Alternatively, it may be evidence that the strongest coupling between the convective and internal wave fields occurs after the convective layer deepens significantly. Subsequent studies by Turner [10], Whitehead and Chen [11], McLaren et al. [12], and Deardorff et al. [13] explored further aspects of penetrative convection, but all of these efforts focused principally on the convective dynamics and characteristics of the transition layer separating the mixed layer from the stratified layer. No particular characterization of the

coupling between convective motions and the internal wave field was provided. McLaren et al. [12] found that the internal waves produced by the penetrative convection had transient characteristics and showed considerable spatial variability. They observed internal wave periods of up to four times the B-V period, although at later times in the experiments the internal wave motion was inclined to oscillate at higher frequencies, nearer to the B-V limit.

Fernando et al. [14] have shown experimental evidence quantifying the growth rate of a convective boundary layer in a non-rotating fluid. They found that the growth law can be written as $h \approx 0.3(q_0 t^3)^{1/2}$, where h is the height of the mixed layer at any time and q_0 the buoyancy flux due to the surface heat flux. Heidt [15] did an experimental study in a penetrative convective system, with particular interest in the growth of the mixed layer and the entrainment of the stratified layer at the boundary of the mixed layer. He derived equations that predict the thickness and temperature of the mixed layer and found a constant empirical factor to characterize the entrainment rate of the interface, which agreed favorably with the meteorological literature.

The aspect ratio of the convection chambers used in these foregoing studies was close to unity so that the existence of a preferred long-wave coupling was somewhat inhibited. The present study differs in that the cell is designed to explore explicitly the convection-wave coupling in an environment where the accessible long waves associated with the planform are clearly distinct and where the longest accessible wave is always large compared to the depth of the mixed layer. As noted in the earlier discussion, it is via the long wave modulation of convection that the coupling between the two distinct dynamics is expected to be most pronounced.

The laboratory experiment reported herein is a model of the atmospheric boundary layer or an inverted version of the upper mixed layer of the ocean, albeit with a no-slip boundary condition at the equivalent free surface of the ocean replacing the (nearly) stress-free atmosphere-ocean interface. The fluid in the convection cell is initially continuously stratified with an essentially constant B-V frequency from the bottom to the top of the cell. The experiment is initiated by rapidly heating the lower boundary whereupon the layer of fluid adjacent to this heated surface quickly becomes unstable. As unstable convective motions ensue, a transition layer appears sandwiched between the turbulent mixed layer and the upper stratified layer. Although the transition layer progressively invades the stratified layer as heat is continually added to the system, this layer is also deformable and responds to both stimuli from convective plumes and from internal waves. Since perturbations of sufficiently low frequency (below the B-V or upper cut-off frequency) at a boundary of a stratified fluid are readily transmitted into the bulk of the stratified domain as propagating internal waves, it is expected that plumes impinging on the transition layer will excite vertically-propagating waves. A more significant dynamical effect, we believe, involves long internal waves which modulate the height and thickness of the transition layer, with a potential for influencing both the convective transport across the layer and the rate of rise of the layer. This work seeks to describe this process starting with initiation of heating and encompassing a time period approaching the asymptotic state determined by the fixed incremental increase in temperature of the lower boundary.

2. Experimental setup and procedures

2.1. The convection cell

The experimental work was performed in a rectangular plexiglas tank (Fig. 1), which had a cross-section of 84.50 cm $\times$ 7.70 cm and 10.70 cm deep (tank walls were 1.80 cm thick). A right-handed Cartesian coordinate system was used to define the orientation of the convection cell. The x-direction is aligned with the length of the cell, the y-direction points horizontally across the width of the cell, and the z-axis points vertically upward. The large aspect ratio (AR $= 8.56$, the length to height ratio) was used to capture many horizontal wavelengths of the convective motion in the x-direction. The top of the convection cell was constructed of plexiglas embedded with six channels for the purpose of allowing recirculating water to flow in alternating directions (anti-parallel). The channels (0.48 cm deep and 0.64 cm wide) were spaced evenly along the top boundary, with the first channel edge aligned with the inside dimension of the convection cell at $y = 0$, and each consecutive channel centerline spaced 1.27 cm from the previous one. This measure was taken in order to keep the top boundary condition uniform. In order to keep heat losses at the ends to a minimum, 2.5 cm thick styrofoam blocks were placed inside the cell, next to the cell ends with 0.63 cm thick plexiglas sheets attached to the block which then became the boundaries for the working fluid.

The lower boundary of the convection cell consisted of an anodized aluminum plate (1.6 cm thick extending the full length of the convection cell) with six embedded water recirculating channels, in a similar configuration as the top boundary. Thermistors were embedded in the lower channel plate (along the x-axis, centered in y) and used to measure the temperature at the lower boundary. Several layers of fiberglass insulating material were placed beneath the lower boundary to minimize heat loss in the $-z$ direction, away from the convection cell.

A layer of styrofoam insulation (24 mm thick) was placed around the convection cell to prevent heat loss during setup time (formation of stable stratification). Part of the insulation layer was removed from both sides of the convection cell (to keep any heat losses symmetric with respect to the center $x-z$ plane) during experimental runs for flow observation.

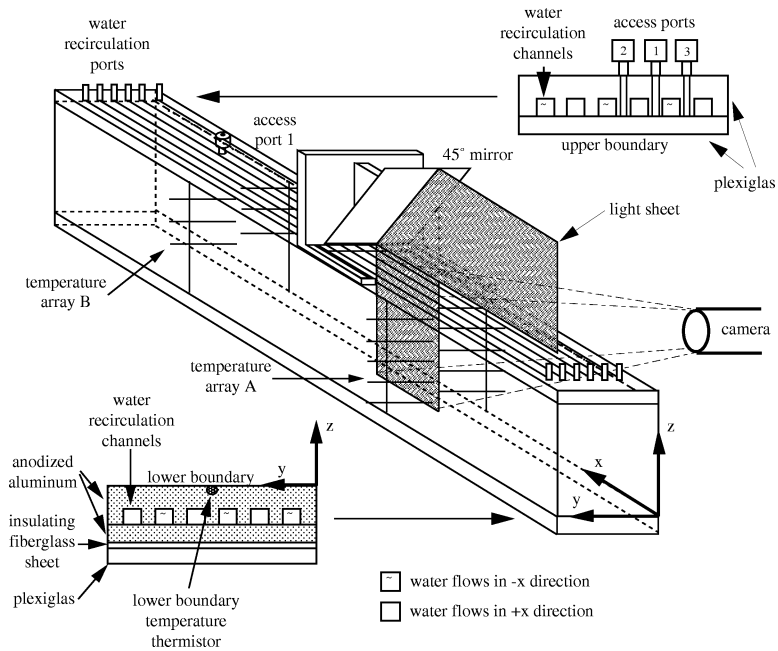

Fig. 1. Convection cell.

Table 1
Properties of the working fluid (water/glycerine at 20 °C)

Physical variable	Symbol	Value
Thermal expansivity	α	2.5×10^{-4} °C^{-1}
Kinematic viscosity	ν	1.006×10^{-2} cm^2/s
Thermal diffusivity	κ	14.33×10^{-4} cm^2/s
Density	ρ	1.047 g/cm^3
Specific heat	c_p	4.1818 J/(g °C)

The top and bottom thermal boundary conditions in the convection cell were created using water recirculators. The initial stratification was setup with two separate digital, constant-temperature recirculators. The bottom boundary was heated above the initial bottom boundary setpoint by a third recirculator (Bath 3) during experimental runs. A more complete description of the experimental setup can be found in Michaelian [16].

2.2. Fluid properties

Deionized water was utilized as the working convection fluid. In addition, 16% to 22% glycerine was added to the deionized water to form a mixture which had a density of $\rho = 1.047$ g/cm^3 in order to match the density of the particles used to make velocity measurements of the flow. This mixture did not change the working fluid viscosity by a significant amount, as the viscosity as a function of the percentage of glycerine is essentially constant up to values approaching 50% glycerine. Table 1 gives more details concerning the characteristics of the fluid.

2.3. Data acquisition

2.3.1. Temperature measurements

Temperature data was acquired by using two temperature probe arrays (Fig. 2). The first array, hereafter referred to as Array $\mathcal{A}$, consisted of ten probes positioned at 1/3 of the cell length ($x = 28.2$ cm). Probe 0 of Array $\mathcal{A}$ was placed a distance $z = 0.95$ cm above the bottom boundary, and each probe thereafter was spaced about one centimeter above its lower neighbor. All temperature probes were aligned mid-way through the convection cell's y-direction, at $y = 3.85$ cm. The probes protruded from alternating sides of the convection cell, so as to prevent asymmetric heat losses. The second temperature array (Array $\mathcal{B}$)

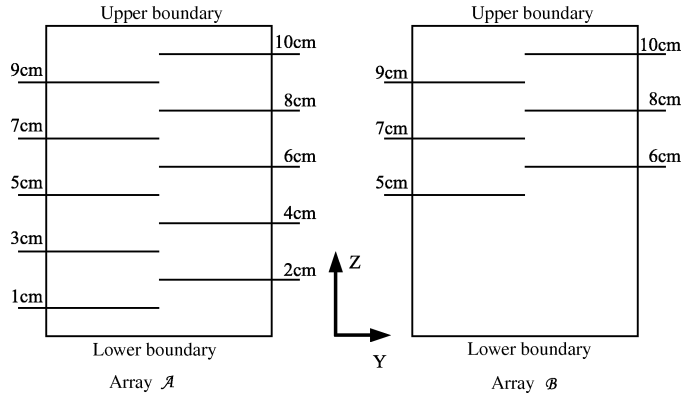

Fig. 2. Temperature probe setup (cross-sectional view); left – Array $\mathcal{A}$, right – Array $\mathcal{B}$.

was positioned at 2/3 of the cell length ($x = 56.8$ cm). Array $\mathcal{B}$ consisted of six probes placed starting at $z = 4.93$ cm, 6.07 cm, 7.02 cm, 8.13 cm, 8.96 cm, and 9.83 cm, respectively.

The thermistors utilized in these experiments had diameters of 0.10 cm and were insulated with teflon. The probes were epoxy-encapsulated, electrically isolated and had time constants of 0.1 sec. The thermistors were calibrated in a series of constant temperature baths. The thermocouples used in the experiments were type E, had diameters of 0.08 cm, time constants of $\approx$0.25 sec, and were calibrated at constant water bath temperatures. The temperature values were found to vary by $\pm 0.01\,^{\circ}$C. All temperature signals were conditioned with a signal conditioning system and stored on an anlog to digital 12-bit acquision board. The vertical temperature arrays were sampled at $\approx$0.5 Hz using a moving average. The moving average consisted of a sampling rate of 1200 Hz and averaging the samples over 1.0 sec. Most runs consisted of 2048 data points taken for each temperature probe over a 34 minute run time.

2.4. Velocity measurements

CIV (Correlation Image Velocimetry) was used to determine the velocity field associated with the flow. At the heart of the CIV scheme (Fincham and Spedding [17]) is the correlation of image pairs, which are used to track groups of particles between frames within a light sheet (0.25 cm thick) which illuminated a specific $x-z$ plane. The thin light sheet was approximately 13 cm in the horizontal (x-direction) and 10.7 cm in the vertical (z-direction). The left-hand corner of the light sheet was placed at $x = 28.2$ cm, at the same position as temperature array $\mathcal{A}$. The light sheet illuminated an $x-z$ plane that was centered at $y = 2.41$ cm (from the convection cell wall). Video image pairs were taken at a certain time delay apart. The series of image pairs were analyzed using a cross-correlation technique to obtain the velocity fields. The velocity data was spline-interpolated to fill in missing gaps/incorrect velocity vectors. This interpolated version of the velocity field was used to obtain all velocity-related statistics of the system. In these experiments, it was common to use box sizes of radius 18–22 pixels, and search radius sizes of 33–50 pixels in the CIV calculations.

Since motions in the convective layer and the stratified layer had different time scales, two separate pairs of images were acquired for each experiment. Image pairs acquired to resolve the convective layer had a time delay of approximately 6 frames (0.20 sec.) and pairs acquired for the stratified layer had a time delay of approximately 40 frames (1.33 sec.) These delay times allowed for displacements of approximately 5–10 pixels in both cases.

Spherical Plyolite AC particles with diameter $106\,\mu\text{m} \leqslant d \leqslant 180\,\mu\text{m}$ were used to visualize the flow. The Plyolite particles had excellent light reflection properties, had an average density of $\rho = 1.047$ g/cm^3, and were approximately neutrally buoyant in the fluid.

CIV velocity measurements were calibrated prior to starting each experiment. The key issue in calibrating the velocity of the neutrally buoyant particles suspended in the working fluid was the size of the video image. The time was known to within 0.01 seconds from the computer clockspeed. However the size of the video image changed slightly between experiments because the depth of field changed. The video image was calibrated with a measurement rule and was stored for later use.

2.5. Heat flux calculations

In these experiments, the heat flux was used as a measure of the forcing function behind the convective motions which penetrate into and interact with wave motions in the stratified layer. The heat flux input was calculated using an energy balance applied to a control volume in the lower mixed layer as shown schematically in Fig. 3(a). The bottom edge of the control

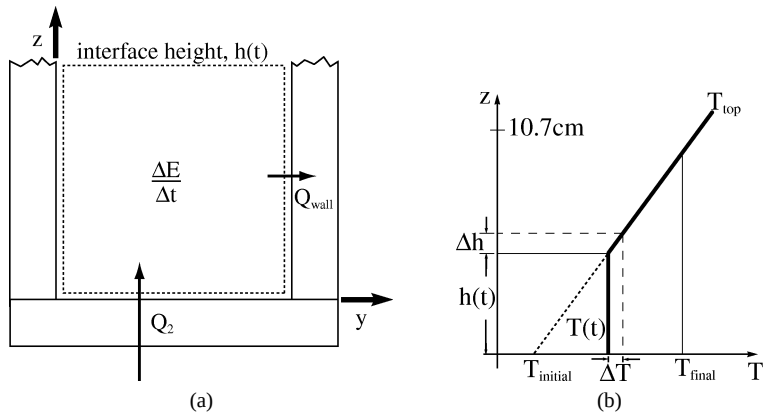

Fig. 3. System energy balance: (a) control volume schematic; (b) internal energy distribution.

volume is positioned along the lower cell boundary and the top of the control volume is positioned at the interface height $h(t)$. The energy balance law for a control volume can be written as

$$Q_2|_t = \left.\frac{\Delta E}{\Delta t}\right|_t + Q_{\text{wall}}|_t \tag{4}$$

and

$$q_2|_t = \frac{Q_2|_t}{A_{\text{cell}}}, \tag{5}$$

where $\Delta E/\Delta t|_t$ is the rate of increase of the internal energy of the working fluid at a specified time, Q_2 is the total conductive heat flux through the lower surface of the convection cell, Q_{wall} is the total heat lost out of the convection cell walls. The conductive heat flux across the moving interface is ignored. Using Fig. 3 as reference, the rate of increase of internal energy can be written as

$$\frac{\Delta E}{\Delta t} = \rho c_p \frac{\mathrm{d}\overline{T}}{\mathrm{d}z} h \frac{\mathrm{d}h}{\mathrm{d}t} A_{\text{cell}}, \tag{6}$$

where c_p is the specific heat, $\mathrm{d}\overline{T}/\mathrm{d}z$ (see section 3.1 for definition of $\overline{T}$) is the background stratification, A_{cell} is the area of the horizontal cross-section of the cell, t is the time, and h is the height of the interface.

2.6. Experimental procedures

A background stratification was formed in the convection cell in order to explore the interactions between turbulent, penetrative convection and internal waves. The stratifications were constructed with the use of temperature-controlled boundary conditions which were utilized to stably stratify the system over a period of time sufficient to form a linear profile. Five different stratifications were implemented for this work with specific details listed in Table 2.

Upon reaching a steady state, a separate, second water recirculator temperature bath was connected to the bottom boundary. The second temperature bath contained water which was hotter than the bath used for stratification purposes. The hot water was

Table 2
Convection/internal wave interaction experiments

Expt.	Initial stratification N [s^{-1}]	ΔT_{str} [°C]	Amt. heat applied % ΔT_{str}	Cell length [cm]
L	0.90	40.0	80	84.5
A	0.78	30.0	80	84.5
C	0.63	20.0	80	84.5
F	0.45	10.0	80	84.5
I	0.32	5.0	80	84.5
H1	0.45	10.0	80	84.5
K1	0.44	10.0	80	84.5

used to heat the lower plate, generating penetrative convection at the base of the stratified layer. The temperature of the second water bath was chosen to be 80% of the temperature difference between the initial stratification temperatures of the top and bottom of the convection cell for all experiments reported here. Hence, the asymptotic height of the interface between the mixed layer and the stratified layer is the same for all experiments.

3. Results and discussion

3.1. Interface rise and thickness

Temperatures measured by the individual probes in Array $\mathcal{A}$ and Array $\mathcal{B}$ were averaged over a sliding time interval of 100 s to obtain a 'mean' temperature at the elevation of each probe. This procedure yielded a slowly-varying (in time) temperature profile $T(z,t)$, the time variation arose because of the advancing interface as convection penetrated into the stratified layer. A fluctuating temperature $T'(z,t)$ is defined relative to the slowly-varying mean temperature $\overline{T}(z,t)$ by subtracting this mean value from the local measured temperature.

Two different methods were used to extract the position of the interface. The first method (Fig. 4(a)) employed the breakpoint of the two straight lines defining the quasi-steady temperature curve at different times during the experiment. Hereafter this method is referred to as 'the temperature breakpoint method'. The second method, hereafter referred to as the 'N^2-maximum-slope method' (Fig. 4(b)), entailed using a least-squares, constrained-spline approximation to fit the temperature versus height curve. This curvefit was differentiated in order to calculate the Brunt-Väisälä (B-V) profile ($N^2 = g\alpha\,\mathrm{d}T/\mathrm{d}z$, where α is the coefficient of thermal expansion). The N^2 curve was differentiated again in order to find the maximum slope of this profile. The level at which the maximum slope occurred was taken to be another characteristic measure of the interface height. At the same time an upper and lower interface boundary could be obtained using the points where the maximum slope of the B-V profile intersected the ordinates $N = 0$ and $N_{\max}$ as shown in Fig. 4(b). The distance between these points defines a slope thickness which was used as a measure of the interface thickness.

The measured characteristics of the interface rise and thickness for a sequence of experiments at different ambient stratifications (Experiments L, C, and I) are shown in Fig. 5. In each case, the interface rises in 'steps', as determined from the N^2 maximum-gradient method. All experiments listed in Table 2 exhibited the same, qualitative movements of the interface. The differences between the various stratified cases lie primarily in the width, depth and number of the steps that the interfacial region locks into while rising. The thickness of the region nominally has three to four peaks as the interface rises during a typical experiment. One possible explanation for this step-like advance of the interface is that the interface region is intermittently 'locked' by long internal wave modes in the cell generated entirely by an intrinsic coupling with convective motions. Another important feature of the interface rise characteristics is the thickness of the interface. The 'interface' has a finite thickness in which the field of active turbulent convection gradually transitions to the stably stratified layer. The thickness of this layer can be thought of as defining the nominal range in the variation of the height of convective plumes. The interface thickness clearly varies in an oscillatory manner as the interface height increases.

The interface rise data based on the temperature-breakpoint method for Experiment L with $N = 0.90\ \mathrm{s}^{-1}$ is shown in Fig. 6. The interface movement in time shows two distinct regions with different power-law variations. These distinct regions were evident in all of the experiments. The initial interface rise rate was defined as Region 1 and the final interface rise rate was defined as Region 2. Power-law fits were formed for each region of the interface rise characteristic for each experiment. The

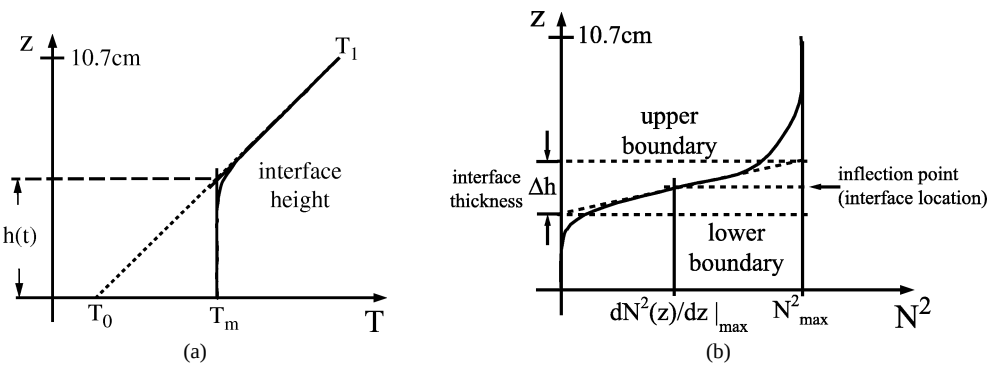

Fig. 4. Methods for calculating interface position: (a) temperature-breakpoint method; (b) N^2-maximum-slope method – also used for calculating interface thickness.

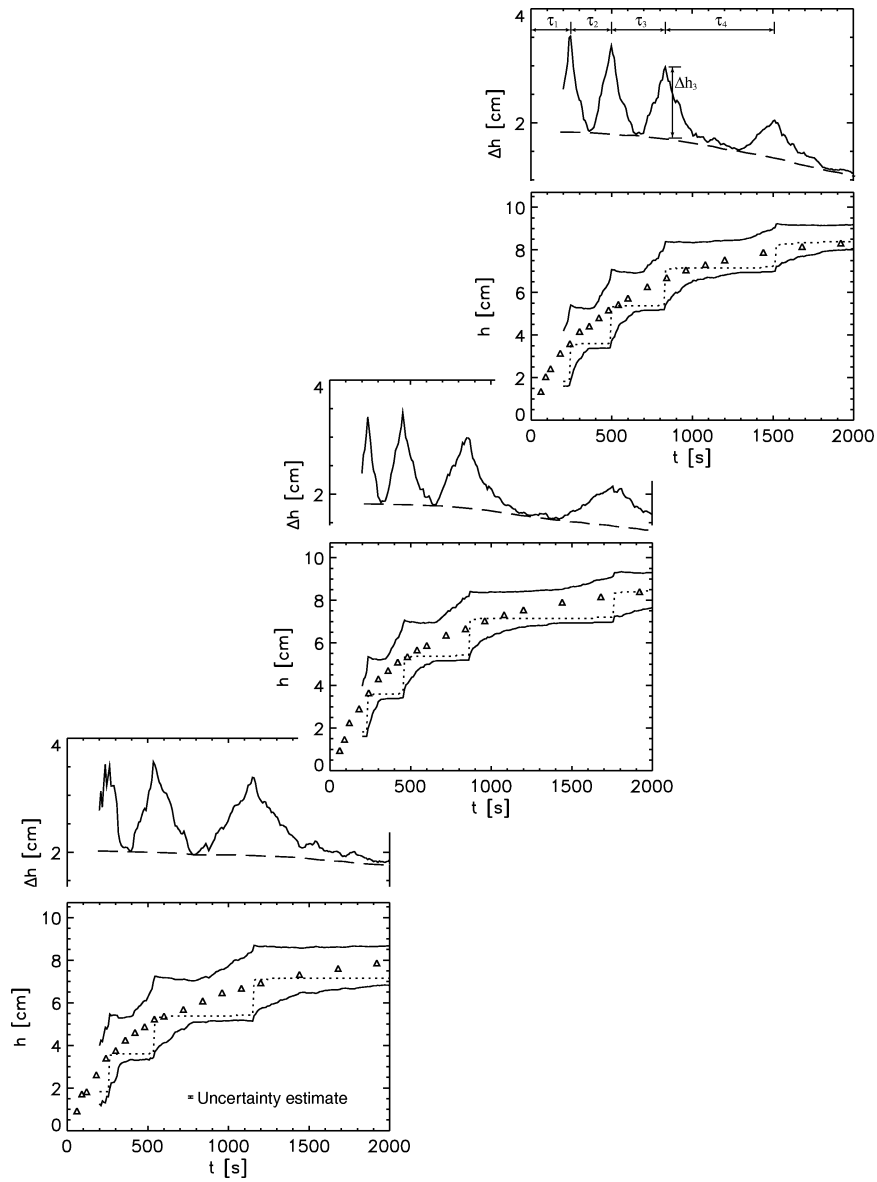

Fig. 5. Interface rise and thickness with respect to time. In each of the three panels there are two plots. The upper plot legend – (—) interface thickness, N^2 maximum-slope-method; (– – –) represents the local minima for the interface thickness. The legend for the lower plot – (· · ·) mean interface height, N^2 maximum-slope-method; (—) interface upper and lower bounds, N^2 maximum-slope-method; (△) mean interface height, temperature-breakpoint-method. Lower panel – Experiment I ($N = 0.32\ \mathrm{s}^{-1}$). Middle panel – Experiment C ($N = 0.63\ \mathrm{s}^{-1}$). Upper panel – Experiment L ($N = 0.90\ \mathrm{s}^{-1}$).

amplitude coefficients for the power law fits are seen in Fig. 7. Region 1 amplitude coefficients remained approximately constant for all stratifications and had a mean value of 0.22. Region 2 coefficients conformed to a linear trend in which the amplitude was related to the stratification according to the law: $\mathrm{Amplitude}(N) = 0.71N + 0.49$. The power law exponents describing the interface rise rate are seen in Fig. 8. The interface rises as $t^{0.52}$ for Region 1 and changes to $t^{0.29}$ for Region 2. The point of transition between the two regions was defined as τ_{break}. The parameter τ_{break} is seen to vary according to the underlying stratification (Fig. 9). This relationship is fitted with a power law and the transition time between Region 1 and 2 to varies according to $N^{0.49} \approx N^{1/2}$. The interface rise rate was similar regardless of the strength of the ambient stratification.

The variation of the interface position (determined by the temperature-breakpoint-method) with respect to time is shown in non-dimensional form in Fig. 10. The interface height is scaled with the asymptotic height h_a, and the time variable is non-

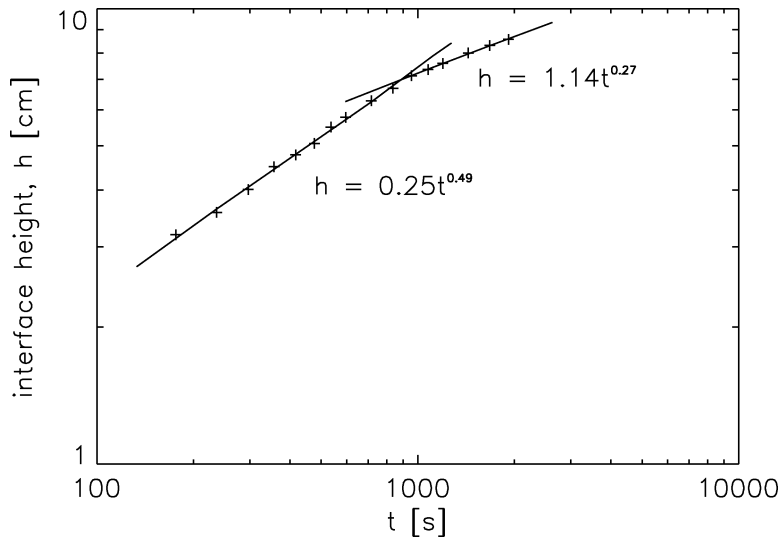

Fig. 6. Interface rise rate for Experiment L ($N = 0.90\ \mathrm{s}^{-1}$).

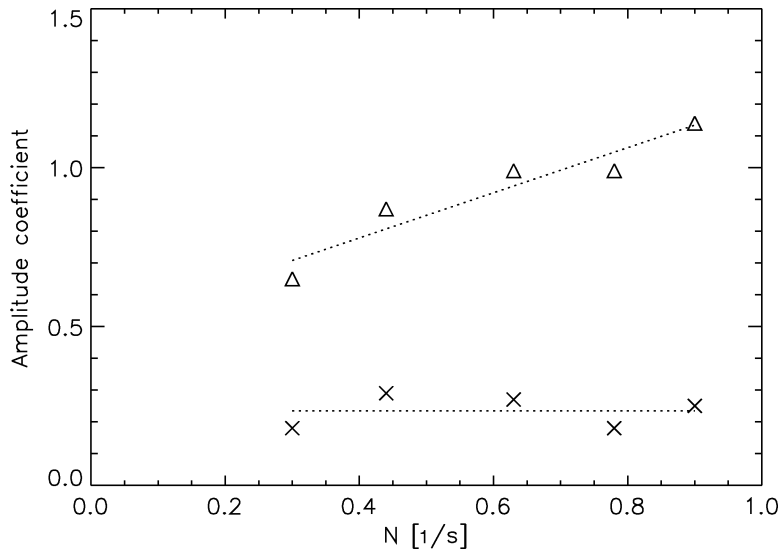

Fig. 7. Stratification effects on interface rise amplitude coefficients. (×) – Region 1 amplitude coefficients, (· · · ·) – average value for Region 1 coefficients (0.22); (△) – Region 2 amplitude coefficients, (· · · ·) – least squares slope for Region 2 coefficients (Amplitude $(N) = 0.71N + 0.49$).

dimensionalized with a diffusion time scale (h_a^2/ν) based on the final asymptotic interface height and the fluid viscosity ν. The final asymptotic interface height h_a is defined as

$$h_a = \frac{T_{b\infty} - T_{b0}}{\frac{\mathrm{d}\bar{T}}{\mathrm{d}z}|_0}.$$

$T_{b\infty}$ is the final asymptotic temperature value assumed by the bottom boundary following the period of active heating (and determined by the fixed temperature of the heating bath); T_{b0} is the initial bottom boundary temperature; and $(\mathrm{d}T/\mathrm{d}z)|_0$ is the initial stratification. Recall that all experiments were designed to have the same value of h_a. The data curves in non-dimensional form collapse onto one another for different stratifications. This reveals the practical utility of the proposed scaling.

Characteristics of the temporal variations in the interface thickness Δh exhibited in Fig. 5 are summarized in Figs. 11 and 12. First, the time intervals τ_i between successive peaks in the interface thickness Δh are displayed in Fig. 11. The time intervals in Fig. 11(a) are normalized by the background stratification time scale, N. The data shown in Fig. 11(b) are normalized by a local diffusion time based on the local mixed layer depth h_p at the time when Δh achieves a particular peak value. Fig. 11(a) reveals

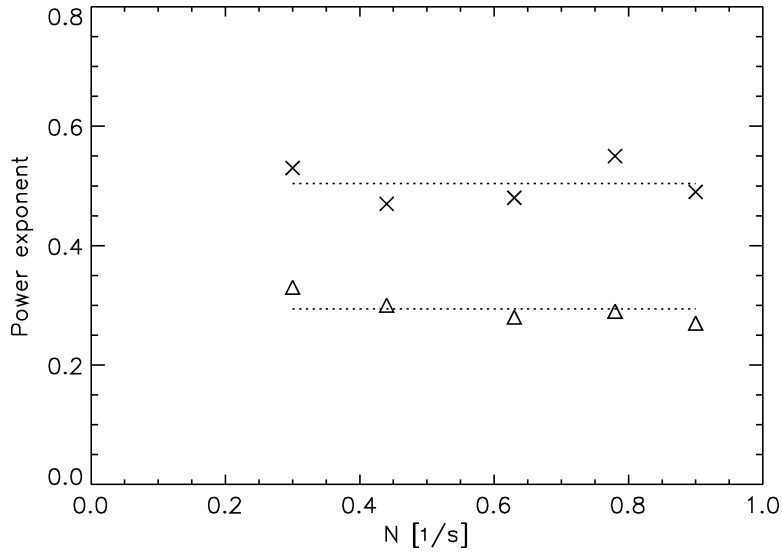

Fig. 8. Stratification effects on interface rise exponent coefficients. (×) – Region 1 exponent coefficients, (· · · ·) – average value for Region 1 coefficients (0.52); (△) – Region 2 exponent coefficients, (· · · ·) – average value for Region 2 coefficients (0.29).

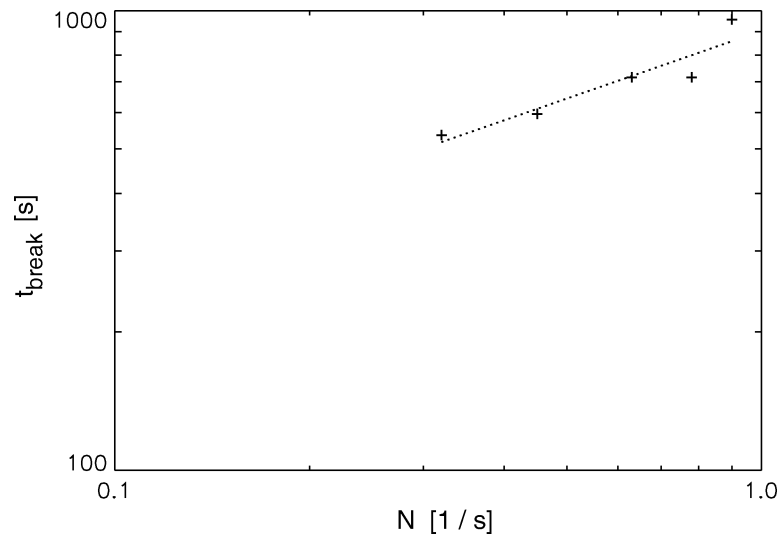

Fig. 9. Effects of stratification on the interface rise break time. Power law fit shows $\tau_{\text{break}} \sim N^{0.49}$.

that the two earliest peaks in Δh occur at the same fixed time over the entire range of stratifications studied. Subsequent peaks, however, appear with increasing time delays as N decreases. Interestingly, the time intervals τ_2 and τ_3 have a quite similar trend with increasing B-V frequency when scaled with the local diffusion time as seen in Fig. 11(b). One might speculate that the earliest and latest peaks shown in Fig. 5 are influenced by the presence of no-slip boundary conditions. The first peak after onset of heating is probably influenced quite strongly by the bottom boundary as is clear from the large values of τ_1 when scaled by the local diffusion time. Similarly, the last peak is influenced, but perhaps not quite to the same extent, by the top surface as the stratified region shrinks to a small fraction of the mixed layer depth. This speculation is supported by the fact that the value of τ_4 in Fig. 11(b) is not far removed from the data for τ_2 and τ_3 at the larger values of N. Even though the stratified layer is already quite thin when the fourth peak in Δh appears at these higher values of N, the top boundary is not yet providing a strong constraint on the dynamics in the interface region.

The extremes in the excursions of the thickness of the interface from a peak to a local minimum are shown in Fig. 12. It appears that the peak-to-minimum excursions in the interface thickness are essentially independent of the stratification of the adjoining layer. Of course, one expects that this trend must fail as N approaches zero, a result suggested by the slight downward

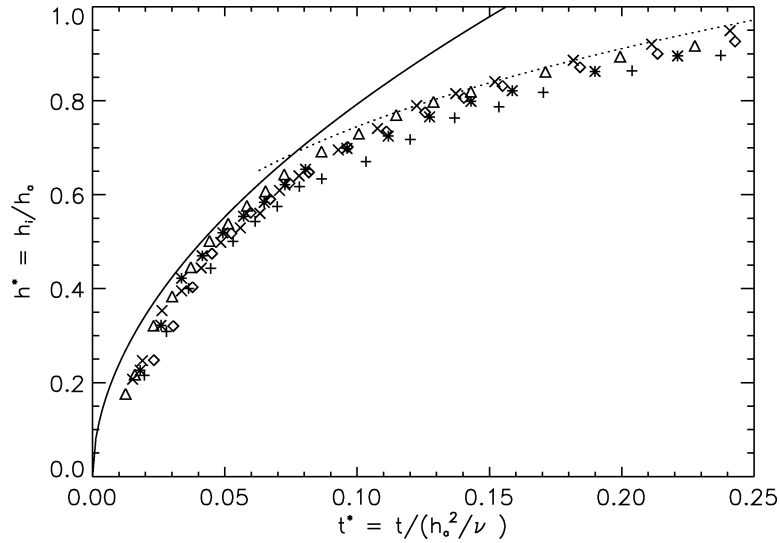

Fig. 10. The variation of the non-dimensional interface rise, h_i/h_a with non-dimensional time, $t/(h_a^2/\nu)$. (——) – Region 1 curvefit, $h^* \sim t^{*0.52}$; $(\cdots)$ – Region 2 curvefit, $h^* \sim t^{*0.29}$; $(\times)$ – experimental data from $N = 0.90\ \mathrm{s}^{-1}$, $(\triangle)$ – experimental data from $N = 0.78\ \mathrm{s}^{-1}$, $(\diamond)$ – experimental data from $N = 0.63\ \mathrm{s}^{-1}$, $(*)$ – experimental data from $N = 0.45\ \mathrm{s}^{-1}$, $(+)$ – experimental data from $N = 0.32\ \mathrm{s}^{-1}$.

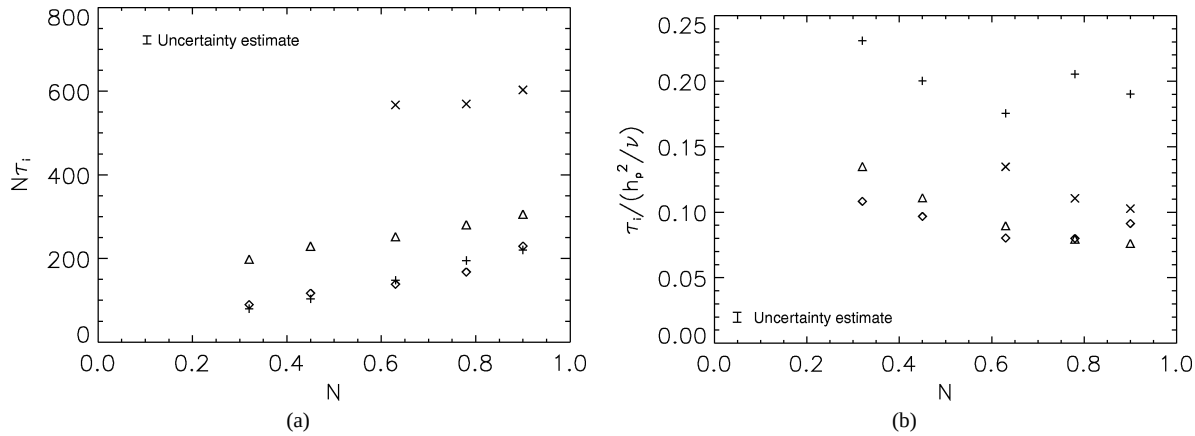

Fig. 11. The effects of stratification on non-dimensional time of appearance, τ_i, between peaks in interface thickness. Legend: $\tau_1 - (+)$; $\tau_2 - (\diamond)$; $\tau_3 - (\triangle)$; $\tau_4 - (\times)$. (a) Stratification time scale is B-V frequency N. (b) Diffusion time scale is based on the local mixed layer depth h_p.

trend in the curves for lower values of N. If, as was speculated above, the dynamics during the time period of the second and third peaks are minimally affected by the boundary conditions, then the scaling for these peaks should be typical of subsequent peaks in deeper cells.

The results in Figs. 11 and 12 raise another issue worthy of comment. Since the indicated trends for the middle two peaks are (essentially) independent of N, one might suggest that the oscillatory modulation of the interface thickness is not necessarily linked to a coupling with long internal waves. This could be argued on the basis that the period of long standing waves in the cell should scale with N, but such a trend is only weakly evident in Fig. 11(b). On the other hand, one might offer a counter argument on the basis that the particular set of long wave modes active in experiments with different N, and constrained by the fixed cell length, may differ sufficiently so as to yield only a mild variation with N, such as indicated by the data shown in Fig. 11(b). Consequently, it is somewhat speculative to appeal to the presence of standing, long internal waves generated by a convection/wave coupling mechanism as the primary explanation for the observed modulation of the interface thickness.

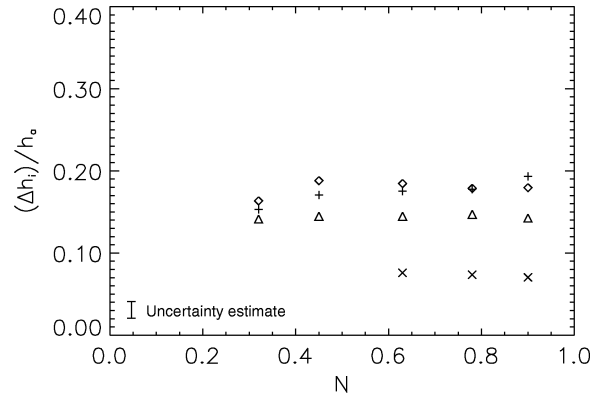

Fig. 12. The effects of stratification on non-dimensional height difference between successive peaks in interface thickness (Δh). Legend: τ_1 – (+); τ_2 – ($\diamond$); τ_3 – ($\triangle$); τ_4 – ($\times$).

3.2. Heat flux

The heat flux is an important measure of the efficiency of convective transport across the mixed layer. As explained in Section 2.5, the heat flux was not measured directly, but was calculated from the energy balance law relating the measured internal energy of the working fluid at a specified time and the heat flux sources and sinks in the system. As such, the applied heating rate has a functional relationship that is dependent on the measured interface rise characteristics exhibited in Fig. 10. Assuming that all the energy transferred across the bottom plate is available to heat the growing convective layer (i.e., neglecting sidewall losses and any conductive flux from the stable layer to the mixed layer), one can write

$$\frac{\mathrm{d}h}{\mathrm{d}t} = \frac{\frac{\partial T_m}{\partial t}}{\frac{\mathrm{d}\overline{T}}{\mathrm{d}z}\big|_0} = \frac{\frac{q}{\rho c_p}}{h\frac{\mathrm{d}\overline{T}}{\mathrm{d}z}\big|_0}, \tag{7}$$

where T_m denotes the (assumed uniform) temperature of the mixed layer. This relation can be written alternatively in the form

$$h^2 = 2\left(\frac{\mathrm{d}\overline{T}}{\mathrm{d}z}\bigg|_0\right)^{-1}\int_0^t \left(\frac{q}{\rho c_p}\right)\mathrm{d}t'. \tag{8}$$

Hence, there exists a one-to-one equivalence between the applied heating rate and the interface rise. For example, a uniform heating rate implies an interface rise, $h \sim t^{1/2}$. A further point about equation (8), and one that should be born in mind relative to the heat flux and temperature data that follows, is the fact that the interface position h depends on a cumulative measure of the local heat flux q. As a consequence, local variations of the internal energy in the mixed layer, reflecting true local variations in the wall heat flux, are not so obviously manifested in terms of local variations of the interface height.

Fig. 13 shows the dimensional heat flux variations during the course of the experiment for each stratification. The figure shows that initially the heat flux across the bottom boundary increases rapidly to a well defined peak value, similar to a 'δ-function like' pulse for the highest stratification. After reaching a global maximum, the heat flux decreases along a path which varies with the strength of the ambient stratification. For the higher stratification experiments, the heat flux 'equilibrated' to a (almost) constant plateau before undergoing another steep decline. When the ambient stratification becomes weaker, the plateau region becomes less-well defined, eventually vanishing entirely. In the tails of the asymptotic decay, as the interface approaches its asymptotic height and the mixed-layer temperature approaches the temperature of the bottom surface, one observes distinct oscillations in the magnitude of the heat flux. In the presence of moderate to strong stratifications, there is evidence of a secondary peak in the heat flux near the termination of the plateau region, and clearly-defined oscillations in the level of the heat flux within the plateau region. The time at which the secondary peak in the heat flux curves appears clearly depends on the strength of the background stratification. Physically, this trend points to the notion that the stratification imposes a 'stiffness' in the response of the stable layer to penetrative motions. As the stratification decreases, the stable layer becomes increasingly more responsive to convective motions which penetrate deeper into the stratified layer before losing their excess buoyancy. As such the coupling between convective motions and internal wave motions occurs earlier after initiation of bottom heating when the stratification is weaker. Of course, as the stratification becomes vanishingly weak any coupling with internal waves must cease. Hence, we expect the coupling between the mixed layer and internal waves in the stratified layer to depend significantly on the strength of the stratification.

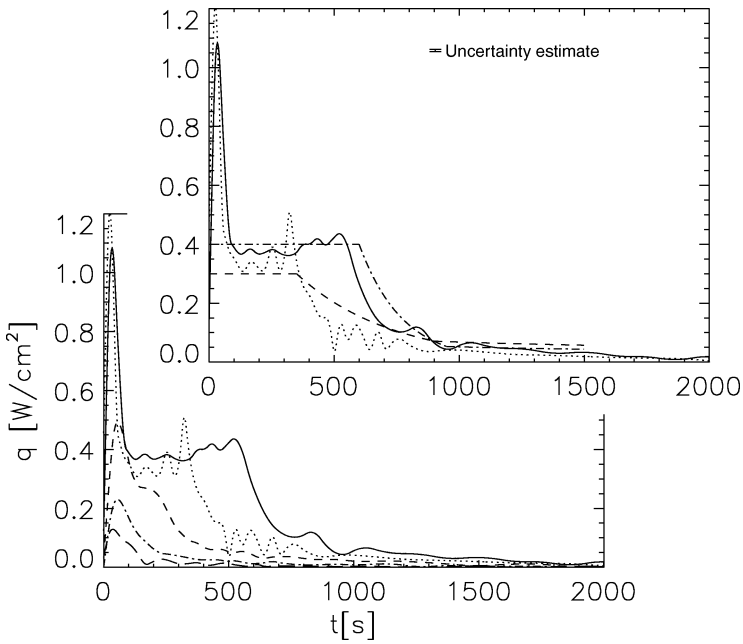

Fig. 13. Heat flux variations in time for various stratifications – dimensional heat flux. Lower left plot: (—) – Experiment L ($N = 0.90\ \mathrm{s}^{-1}$); ($\cdots$) – Experiment A ($N = 0.78\ \mathrm{s}^{-1}$); ($- - -$) – Experiment C ($N = 0.63\ \mathrm{s}^{-1}$); ($- \cdot -$) – Experiment F ($N = 0.45\ \mathrm{s}^{-1}$); (— —) – Experiment I ($N = 0.32\ \mathrm{s}^{-1}$). Inset plot: The same data showing heat flux variations for the two highest stratifications in conjunction with the modeled heat flux curves (from equation (9)). (—) – data, Experiment L ($N = 0.90\ \mathrm{s}^{-1}$); ($- \cdot -$) – modeled heat flux, Experiment L; ($\cdots$) – data, Experiment C ($N = 0.63\ \mathrm{s}^{-1}$); ($- - -$) – modeled heat flux, Experiment C.

Variation of the heat flux with stratification is shown in a different light in the inset portion of Fig. 13. The overlay lines drawn in the figure define the heat flux profiles, computed from equation (8), consistent with interface rise data shown in Figs. 6–9 for Experiments L and C. Clearly there is a transition from a constant heat flux boundary condition to one of continually-varying mixed type after the early period $0 < t < t_1$. The temporal variation of the heat flux was taken in the form

$$q(t) = \begin{cases} q_0, & 0 < t < t_1; \\ q_0 \exp(-\beta_1 (t - t_1)), & t_1 < t < t_2; \\ q_2 \left(\frac{t_2}{t}\right)^{\beta_2}, & t > t_2\ . \end{cases} \tag{9}$$

The constant heat flux q_0 over the interval $0 < t < t_1$ is consistent with the interface rise $h \sim t^{1/2}$ during this early part of the experiment. The variation $q \sim t^{-\beta_2}$ for $t > t_2$ is consistent with the interface rise $h \sim t^{(1-\beta_2)/2} = t^{0.29}$ over the late stages of the experiment. The times t_1 and t_2 were selected from data like that shown in Fig. 6, the specific values chosen carefully as the break times when the data began to noticeably depart from the straight line curves for Region 1 and Region 2 respectively. The values used in Experiments L and A for the parameters t_1 and t_2 are as follows: (1) Experiment L: $t_1 = 600$ s, $t_2 = 950$ s; and (2) Experiment C: $t_1 = 350$ s, $t_2 = 900$ s. Continuity of the heat flux curve required

$$\beta_1 = \frac{1}{t_2 - t_1} \ln\left(\frac{q_0}{q_2}\right). \tag{10}$$

This leaves only one free parameter (alternatively q_2 or β_1) which was subsequently fixed by requiring the total heat flux defined by the curve fit (equation (9)) and the measured data in the interval $0 < t < 1500$ s to coincide. The curve fit yields a reasonable characterization of the temporally-varying heat flux in the experiment.

3.3. Temperature variance

The variance of the fluctuating temperature T' is an indicator of both active convective motion in the mixed layer and of internal wave motion in the stratified layer. Figs. 14–16 show measurements of the temperature variance for the experiments corresponding to the interface data presented in Fig. 5. These figures are organized according to increasing vertical position (at each successive temperature probe), from top to bottom and left to right. The temperature variance was computed using a small window in time ($\mathrm{d}t = 80$ s). The fluctuating temperature in the window was squared, then averaged and plotted versus

time. Noted on the figures are the locations of the interface with respect to time as determined by both interface height methods. The temporally varying interface thickness is represented by the dotted lines ($\cdots$). The position of the interface (from the temperature breakpoint method) is represented by the dashed lines ($- - -$). The interface position and thickness are overlayed in the figures in order to highlight the region of any particular variance record: in the mixed layer (convective motion), in the interface region (combined convective and internal wave motion), or in the stratified layer (internal wave motion). For any particular panel in each figure, the domain to the left of the first dotted line (in time) representing the upper boundary of the interface region is within the stratified layer, while the domain to the right of the second dotted line (in time) representing the lower boundary of the interface region is within the convective layer at each respective height. The domain between these dotted lines show where the fluctuations within the transition layer affect the temperature variance records.

The strongest temperature fluctuations occur near the heated surface and in the transition region around the tips of the plumes. This is clearly borne out in Fig. 14 where a large value of the temperature variance is measured at $z = 0.94$ cm around $t = 350$ s and also at the probe level $z = 6.96$ cm around $t = 750$ s. This latter level is anomalously high compared to values measured at all times and at all probe levels removed from the immediate vicinity of the heated surface. Reference to the top panel of Fig. 5 reveals that the occurrence of the high value of the variance at $z = 6.96$ cm coincides with the third peak in the interface thickness and corresponding step-like rise in the interface position. The probe level $z = 6.96$ cm at this time is intermediate between the upper and lower boundaries of the transition region and is very close to the level of the mean interface position. As shown later (cf. Fig. 23), this space-time location also corresponds to a strong structural change in the frequency spectrum. The dominant frequency peak (i.e., track 1) drops markedly and two new peaks emerge (i.e., tracks 3 and 4). The coincidence of the large variance and structural changes in the frequency spectrum in the stratified layer argues in favor of coupled dynamics. There is some evidence of a mild peak in the variance measured at the levels $z = 8.94$ cm and $z = 9.85$ cm in the stratified layer around this time (i.e., $t = 800$ s), but no particularly strong evidence of energetic wave activity. Of course, the superposition of several internal wave modes with different frequencies and different nodal points in the stratified layer might not be inconsistent with the data.

A somewhat similar behavior is seen in Fig. 15 where a quite high value of the variance was also measured at the level $z = 6.96$ cm and around $t = 950$ s while the probe was in the transition layer. However, the occurrence of the peak variance at this level does not correspond to a peak in the interface thickness nor a time when structural changes occurred in the frequency spectrum. On the other hand, reference to the panel in Fig. 15 corresponding to probe level $z = 8.15$ cm, and related interface data in the middle plate of Fig. 5, reveals that the peak variance at this probe position around $t = 1750$ s does correspond to

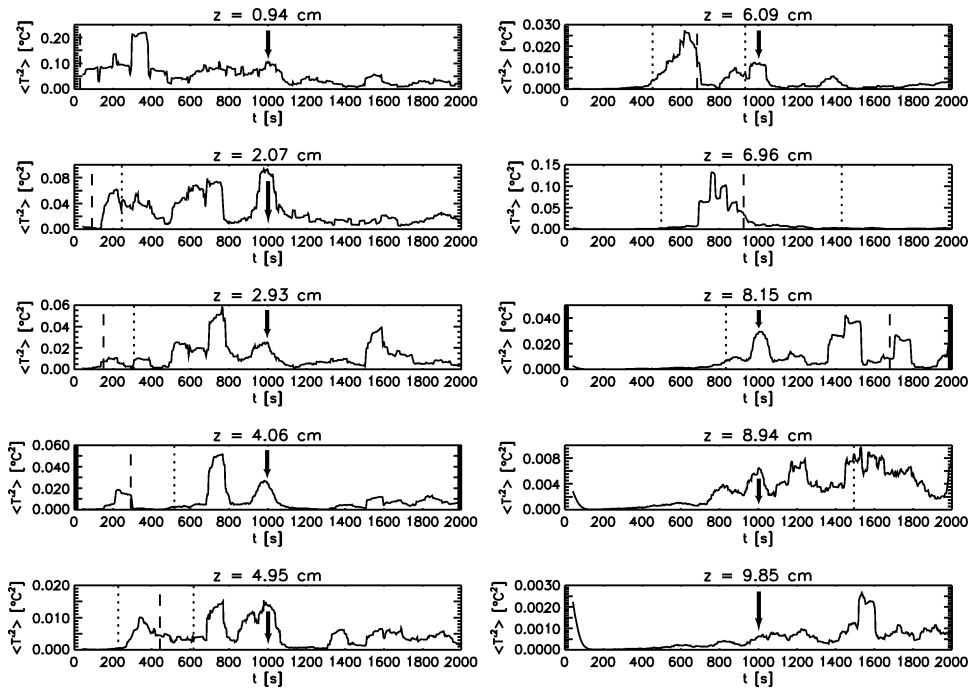

Fig. 14. Experiment L: ($N = 0.90\ \mathrm{s}^{-1}$) Fluctuating temperature variance at various vertical positions. Legend: ($\cdots$) – interface boundaries; ($- - -$) – interface location (temperature-breakpoint method). Figure is ordered in ascending vertical position – top to bottom, left to right. Arrows indicate an event correlated at different cell depths. Note that the vertical scale varies from panel to panel.

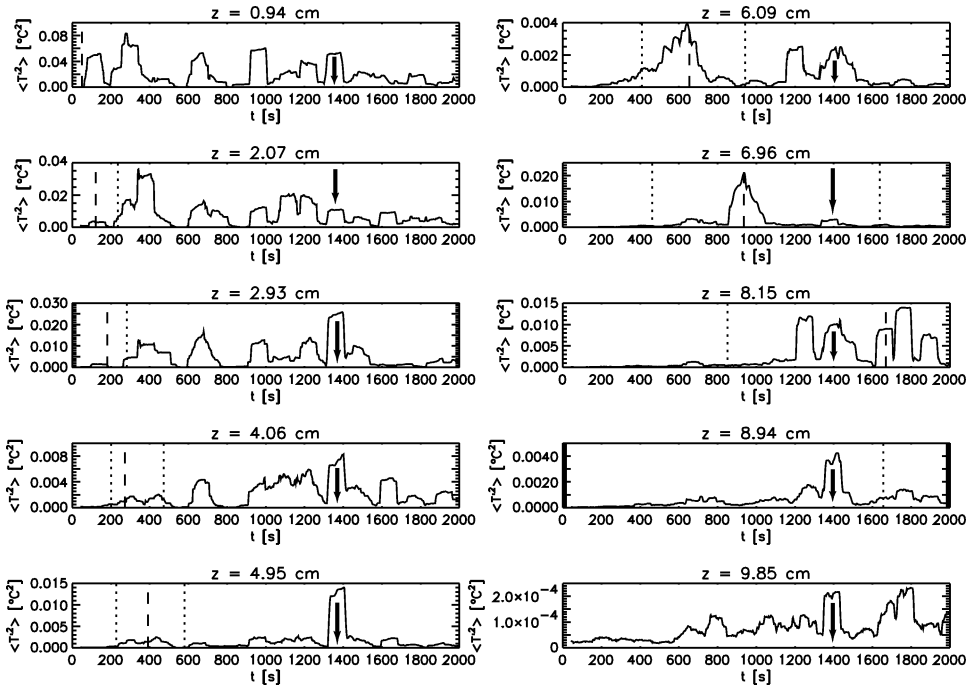

Fig. 15. Temperature variance for Experiment C: ($N = 0.63\ \mathrm{s}^{-1}$). For legend, see Fig. 14.

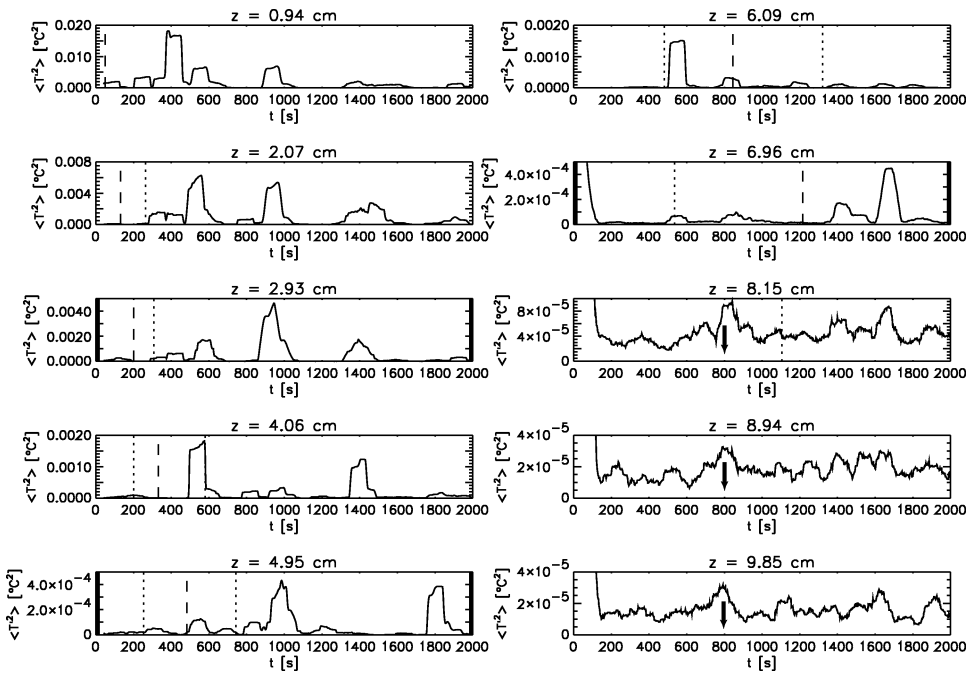

Fig. 16. Temperature variance for Experiment I: ($N = 0.32\ \mathrm{s}^{-1}$). For legend, see Fig. 14.

a step-like change in the interface level as determined by the inflection point in the N^2 profile. Examination of data for other experiments listed in Table 2 quite consistently suggests that the step-like changes in the inflection point of the N^2 profile is accompanied by a comparatively high variance within the interface region, at least when the interface is removed from the constraining influence of the lower surface.

The temperature variance data shown in Figs. 14–16 also reveal episodes of active internal wave activity. Some of the more prominent episodes are marked by a downward arrow on the figures where locally high levels of the temperature variance appear across the stratified region over time scales commensurate with several long wave periods. The fact that intermediate levels sometime exist where the variance is quite small may be attributable to the presence of nodal levels in the eigenfunctions and phase differences in the superposition of several standing waves. The local peak marked around $t = 800$ s on Fig. 16 extends well into the stratified region and exists when the interface is positioned around 5.5 cm above the bottom surface. At this interface level, the convective dynamics are not so constrained by the no-slip boundary condition at the base of the mixed layer and the possible phase instability associated with the intrinsic coupling of convection and waves may have a growth rate sufficient to persist for a period of time before the layer depths change sufficiently to shut off that particular instability mode.

3.3.1. Mixed layer characteristics

Vector fields of the velocity in a given plane were measured at different times to give a more complete understanding of the turbulent plumes and eddies which penetrate into the stratified layer and provide the forcing needed for internal wave

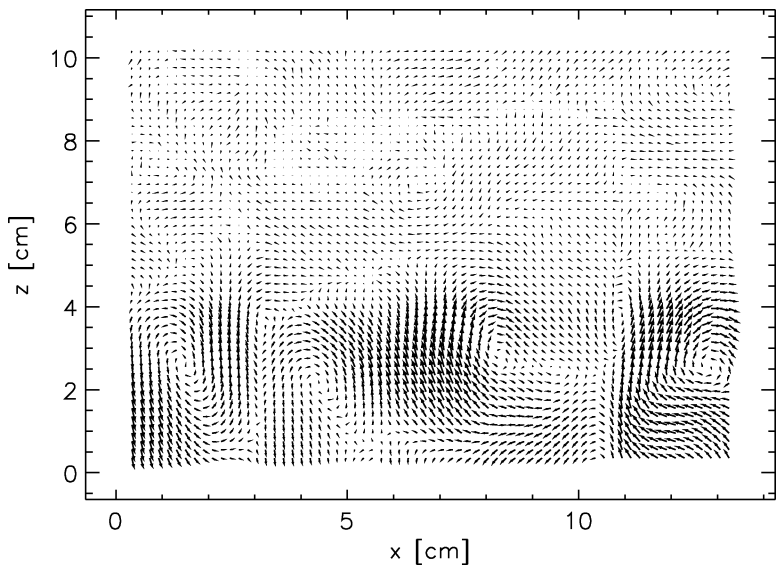

Fig. 17. Vertical velocity vector field ($x-z$ plane) scaled to emphasize motion in the mixed layer for Experiment L ($N = 0.90$ s^{-1}).

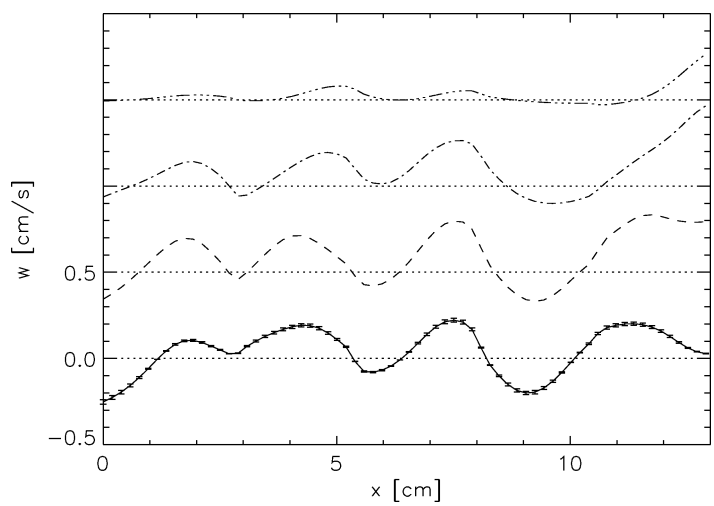

Fig. 18. Experiment L ($N = 0.90$ s^{-1}): Vertical velocity profiles for different z locations in the mixed layer at a fixed time, $t = 261$ s. Legend: (——) – $z = 1$ cm; (– – –) – $z = 2$ cm; (– · –) – $z = 3$ cm; (– · · · –) – $z = 4$ cm. Uncertainty estimate in velocity included on curve for $z = 1$ cm.

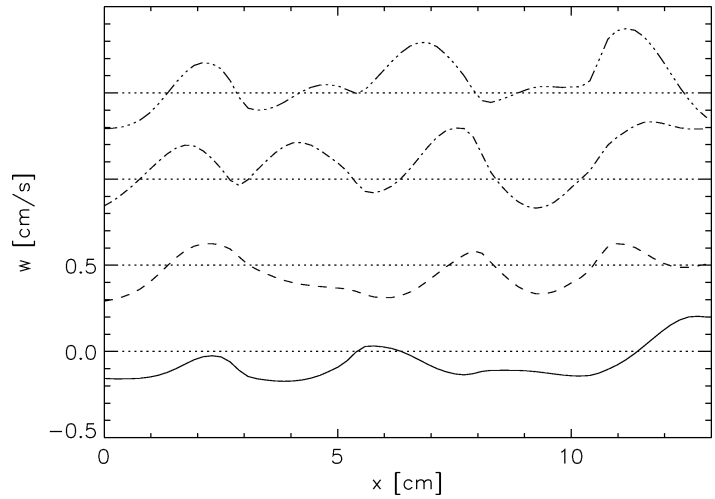

Fig. 19. Experiment L ($N = 0.90\ \mathrm{s}^{-1}$): Vertical velocity profiles for different times at fixed height, $z = 2$cm. Legend: (—) – $t = 237$ s; (– – –) – $t = 249$ s; (– · –) – $t = 261$ s; (– · · · –) – $t = 273$ s.

motion. Fig. 17 shows a resolved CIV measurement for Experiment L ($N = 0.90\ \mathrm{s}^{-1}$). The mixed layer motions are vortical and plume-like in nature, while the stratified layer motions are much weaker. The time scales for motions in the stratified layer are considerably greater than that in the mixed layer and, as a result, the CIV parameters had to be tuned to focus on either the mixed layer or the stratified layer separately. Vertical velocity profiles (from the same data set) at different z positions in the mixed layer taken at a constant time ($t = 261$ s) are seen in Fig. 18. The peaks and valleys of the vertical velocity are correlated from each z position to the next. The wavelength for the vertical velocity peaks for the naturally forced case was nearly 4 cm. Fig. 19 shows how vertical velocity profiles change in time at a constant value of $z = 2$ cm (in the mixed layer for the duration of times shown). It is clear from the figure that the naturally forced case also has fairly strong horizontal movements of peaks. An example of this feature is seen in the middle peak at $x = 8$ cm, $t = 249$ s. This peak moves to $x = 7.5$ cm, at $t = 261$ s, and finally moves to $x = 7$ cm at $t = 273$ s. A first order approximation of the horizontal velocities of the plume-like motions in the mixed layer are in the range of 0.04 cms^{-1}. Such horizontal motions are evidence of the influence of internal wave motions on the mixed layer.

3.3.2. Stratified layer characteristics

Internal wave motions in the stratified layer were also quantified using the CIV method. The motions in the stratified layer fell into two distinct categories. The first category are short wavelength, higher frequency, vertically propagating internal waves. The second category are long wavelength, lower frequency, horizontally propagating internal waves.

The higher frequency internal waves of the first category can be seen in Fig. 20. This figure shows a very regular wave pattern propagating away from a disturbance (a penetrative convective plume) at a specified angle. The angle is designated by velocity vectors which are parallel, yet move in opposite directions. These anti-parallel particle motions are perpendicular to the wave number vector of the internal wave motions within the stratified layer. The frequency of internal wave motion in a uniformly stratified fluid is

$$\omega = N|\cos\theta|, \tag{11}$$

where N is the B-V frequency and θ is the angle made by the wave vector with respect to the horizontal. The group velocity and particle velocities are oriented perpendicular to the wave vector for internal waves. A 'shadow' of the plume disturbance is seen in this figure rather than the plume disturbance itself because the CIV computation parameters were tuned for capturing the internal wave motion, which is on a much slower time scale than that of the convective motions in the mixed layer. The angle of the group velocity (lines parallel to the velocity vectors) in this case is $\theta = 35° \pm 5°$. The wave vector angles are quantified using an angle autocorrelation procedure which focuses on particle motions which have a π phase shift between them (cf. lower plot of Fig. 20). The internal wave angles of propagation, and thus the frequency for the different stratifications are plotted in Fig. 21. The data shown here pertain to early phases of the experiment before the stratified layer becomes thin relative to the mixed layer. An interesting result from this figure is that the angle of propagation is constant (within the experimental uncertainties, as noted on the figure) over the range of stratifications shown. The data sets were taken from experiments at different times. The figure, therefore, reveals that the shortwave frequencies, at least for the early times, appear to be a fixed multiple of the background B-V frequency.

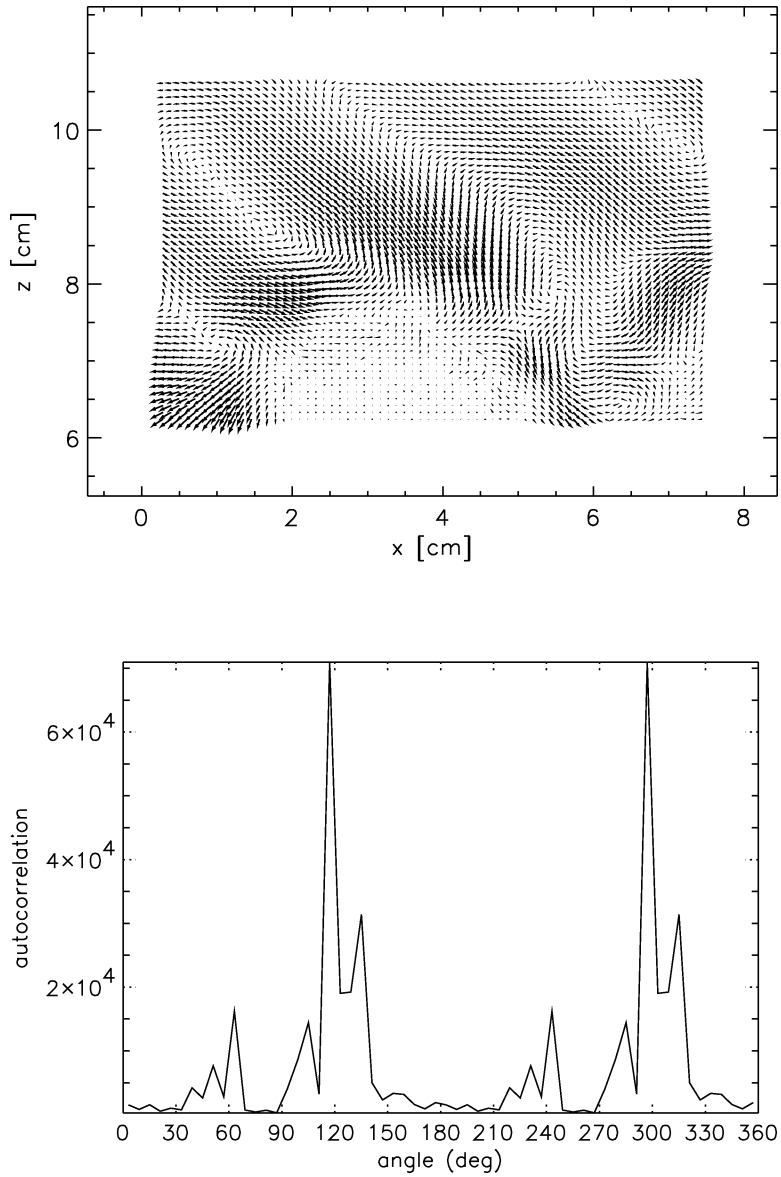

Fig. 20. Top: Velocity vectors scaled to emphasize motion in the stratified layer, showing evidence of shortwave motion for Experiment H1, $N = 0.45\ \mathrm{s}^{-1}$ at $t = 360$ s. Vectors associated with convection have been removed. Bottom: Correlation used to quantify wave vector angle θ in Experiment H1.

Evidence of the second category of internal waves is seen in Fig. 22. The strongest amplitudes of the wave motion for the long internal waves are seen in the figure closest to the interfacial region which lies in between the stratified and mixed layers. The predominant nearly horizontal phase lines indicate a group velocity vector angle of nearly 90° and thus very low frequency long wave motion.

It was observed that the internal wave motion within the stratified layer was intermittent in nature, combining high and lower frequency waves. A typical data set alternately contained periods of strong and weak wave motion.

3.4. Internal wave spectra

Any penetrative convection process must be time dependent since the mixed layer deepens progressively. Consequently, the characteristics of the wave guide are time dependent as well. As long as the mixed layer depth remains a small fraction of the

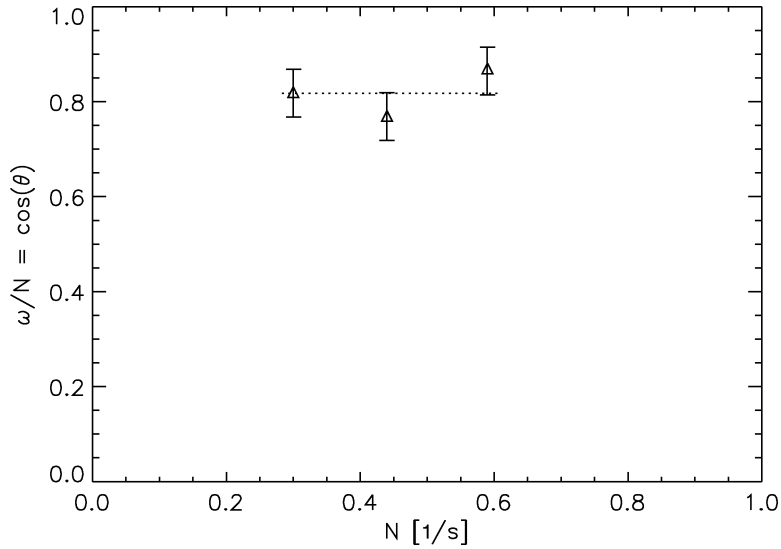

Fig. 21. Variation of internal shortwave propagation angle with stratification.

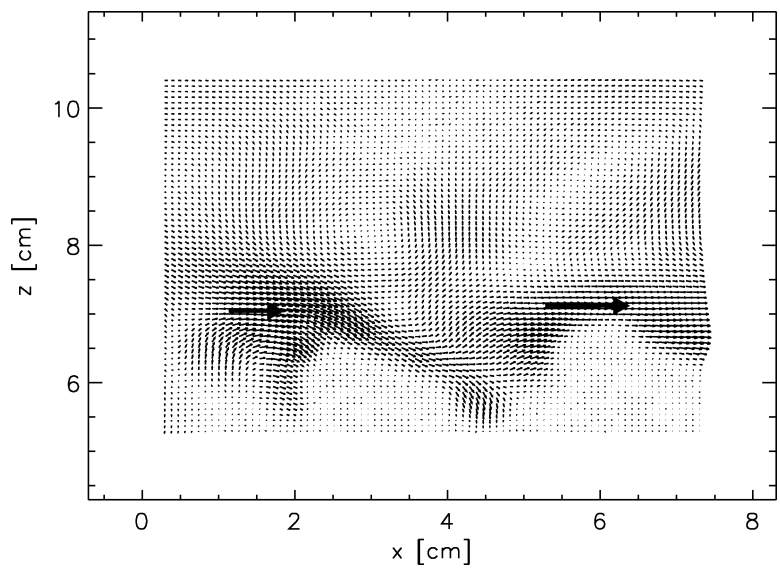

Fig. 22. Velocity vectors showing evidence of longwave motion in stratified layer for Experiment K1, $N = 0.44\ \mathrm{s}^{-1}$ at $t = 431$ s. Note the nearly horizontal vectors which reside near the top edge of the mixed layer – these represent the longwave motion in the stratified layer.

vertical scale of the internal wave guide, any associated internal wave characteristics will be (nearly) stationary. However, when the fractional depth changes of the mixed layer and the internal wave guide are commensurate, the associated internal wave field will exhibit significant temporal variations in both the spectrum and the modal content. Such is the case in the present experiment in a shallow cell where the asymptotic depth of the mixed layer is 80% of the cell depth.

The time-dependence of the experimental system is seen clearly in the variation of the depths of the mixed and stratified layers as shown in Fig. 10. Since the spectral and modal content of the internal wave motion is related to the physical thickness of the stratified layer, the internal wave frequencies present in the layer will also vary with time.

Fig. 23 gives results of the variation in time of individual peaks in the frequency spectrum for the experiment with the strongest background B-V frequency of $N = 0.90\ \mathrm{s}^{-1}$. Peak frequencies were computed using a sliding window FFT applied to the experimental data. The figure shows that the peak frequencies all increase with time. During the course of an experiment, the mixed layer becomes deeper at the expense of the receding stratified layer. The frequency can, therefore, be expected to increase as the depth of the waveguide for internal wave motion in the stratified layer becomes smaller, thus allowing for higher

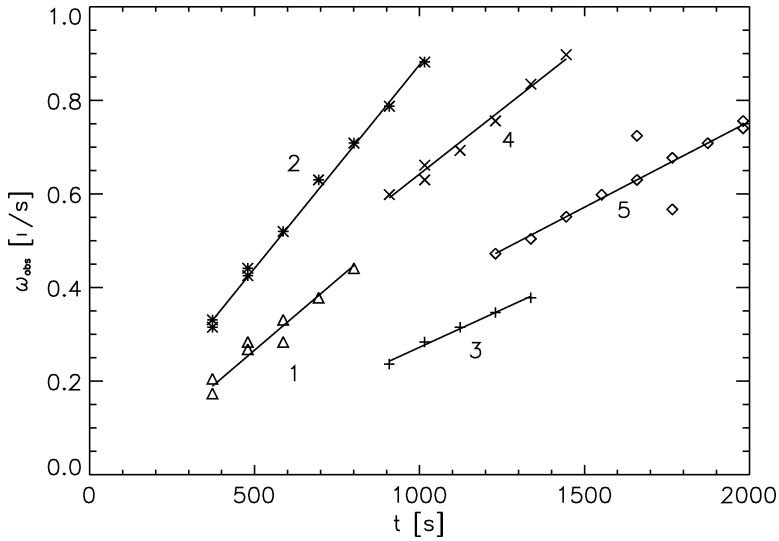

Fig. 23. Experiment L: Frequency variations with time ($N = 0.90\ \mathrm{s}^{-1}$). Legend: ($\triangle$) – frequency track 1 ($\partial\omega_1/\partial t = 0.00060$); ($*$) – frequency track 2 ($\partial\omega_2/\partial t = 0.00087$); ($+$) – frequency track 3 ($\partial\omega_3/\partial t = 0.00032$); ($\times$) – frequency track 4 ($\partial\omega_4/\partial t = 0.00055$); ($\diamond$) – frequency track 5 ($\partial\omega_5/\partial t = 0.00037$).

frequency internal waves in the layer. It is shown in the Appendix in the context of an externally imposed seiche that the variation of frequency is well described by wave kinematics.

As shown in Fig. 26 in the Appendix, individual peaks in the frequency spectrum could be tracked for extensive time periods, and $\mathrm{d}\omega/\mathrm{d}t$ is directly related to $\mathrm{d}h/\mathrm{d}t$. The similarity between the frequency tracks in Fig. 23 and Fig. 26 suggests that both sets of data arise through similar dynamical mechanisms. For this reason, a modal analysis of the internal wave field was carried out in the simpler context of a seiche-forced experiment with the goal of illuminating the connection of these frequency tracks to the presence of slowly-varying, discrete internal wave modes. The primary advantage of the forced long wave experiment described in the Appendix is the coherence and simplicity of the internal wave field in early stages of the experiment. This allows a definitive, quantitative analysis of the internal wave field in terms of only a few of the lowest modes, and the ability to relate this field to measured frequency spectra.

A further noteworthy point regarding Fig. 23 is that several peak frequencies exist simultaneously in the stratified layer at any given time. These peaks appear spontaneously and are reminiscent of the peaks oberved in the forced experiment described in the Appendix after the seiche had decayed. The peak frequencies are tracked with a numbering system. From 350 to 800 seconds, tracks 1 and 2 contain the most energy in the internal wave field, with track 2 continuing on to 1000 seconds. At 900–1000 seconds, tracks 3 and 4 join track 2 as the dominant frequencies in the internal wave field. Evidence from the figure indicates that internal waves propagate at preferred frequencies which, based on results presented in the Appendix, probably correspond to a few of the lowest vertical eigenmodes with discrete wavelengths determined by the longest dimension of the cell. As the layers develop in time, however, the peak frequencies along a specific track begin to decrease and eventually die out, with new peak frequencies becoming dominant. Energy in the internal wave spectrum is forced to flow to different modes in this way, with certain modes dominant until the stratified layer thickness is reduced sufficiently for the system to lock into a different set of modes at a new, lower frequency.

It was shown earlier that the drop-out of track 1, and the emergence of tracks 2 and 3, was associated with a local peak in the thickness of the transition layer and a large temperature variance. We note here that the drop-out of track 4, and the slightly earlier drop-out of track 3, occurs around the time of the final peak in the interface thickness shown in the top plate of Fig. 5. Of course, this occurs quite late in the experiment as the interface is approaching its asymptotic level. We suspect that if the cell were deeper, new frequency tracks would appear. Nevertheless, there appears to be a fairly persistent connection between characteristics of the convection field and the internal wave field.

4. Concluding remarks

Several conclusions from the experiments described here are worthy of further comment. The deepening rate of the mixed layer is seen to be reduced by a combination of low and high frequency internal waves in the interface/stratified layer. As we

compare our experimental results with those from related experiments and theoretical approaches, we observe many similarities. Linden [18] used an oscillating grid to generate a turbulent mixed layer which penetrated into a stratified layer. He showed analytically that the depth of the mixed layer from the grid varied according to $t^{1/2}$ for initial stages of growth and varied like $t^{1/3}$ during the later stages. His inclusion of the kinetic energy production rate explicitly showed $h \propto t^{2/13}$ for early times in the experiment and $h \propto t^{2/15}$ for later times. Kato and Phillips [19] used a different mechanism to model the shear stress at the surface of a stratified layer. In addition to turbulence (created by a grid in the case of Linden [18]), the applied shear stress generated a mean flow. The interface depth for these experiments grew as $t^{1/3}$. Niiler [20] used a model for the response of the upper ocean to surface stress and made theoretical predictions that, for initial mixed layer development, the layer depth varied as $t^{1/2}$. Denman [21] gives theoretical estimates for the mixed layer deepening rate at later times, finding that $h \propto t^{1/3}$.

Our present experiments, which show a mixed layer that deepens intially proportional to $t^{0.52}$ and at later times proportional to $t^{0.29}$, are based upon a mixed layer generated by turbulent plumes and eddy structures. The generating mechanism is an approximation to that of the upper mixed layer of the ocean. Although we fall short in modelling the real oceanic stress-free boundary conditions in our convection tank, we do find good agreement with our results and the results found for other generating mechanisms.

We suggest a possible explanation for the observed reduction in mixed layer deepening rates seen in our experiments as well as in the other results mentioned. During early stages of mixed-layer growth, the dominant forcing function to the system is intermittent plumes and eddies which emanate from along the entire bottom boundary. As these plumes penetrate the base of the stratified layer, they radiate energy into mostly high frequency internal waves. We see evidence of these higher frequency waves from the sliding windowed FFT's seen in tracks 1 and 2 of Fig. 23 during early experimental times. As the layer grows, however, the higher frequency internal waves give way to lower frequency waves which effectively form a mean flow, albeit a weak one in the case of our experiments. The dominant frequency tracks in Fig. 23 begin to transition to lower frequencies at around 900 s, which also happens to be the same time when the interface deepening transitions from its initial growth rate to $h \propto t^{0.29}$. We see additional evidence of this from the temperature variance records (Fig. 14) which show wave activity in the stratified layer after this interface growth transition at ≈900 s. This weak mean flow associated with long internal waves begins to organize the plume motions which were previously observed to be more random. This organization is evidenced by the high correlation of mixed layer motion with the long internal waves seen around 1000 s. As suggested by Linden [18], this reduction of the mixed layer growth rate is most probably caused as a result of energy being radiated away from the top of turbulent layer. We suggest, in addition, that the long wave motion reorganizes the plumes/eddies so that they move horizontally (cf. Fig. 19), as opposed to having predominantly vertical motion at early times. In our experiments, we also note that variations of the heat flux support the idea of mixed layer plumes/eddies moving horizontally. Denman and Miyake [22] observed a combination of short and long period internal waves (varying from the B-V period of 1–10 min to the local inertial period of nearly 16 h) in the northeast Pacific ocean at Ocean Station Papa and note their impact upon the variation in mixed layer depth. Linden [18] also points to the importance of internal waves affecting the dynamics of the upper mixed layer, as well as the mixed layer deepening itself being a possible important source of energy for internal waves in the deep ocean. We note here that this result and explanantion is at odds with the experimental results of Deardorff [13], which showed that the energy drain by internal waves is too small to alter the deepening of the mixed layer.

The time at which the mixed layer deepening transitions from $h \propto t^{0.52}$ to $h \propto t^{0.29}$ is proportional to $N^{1/2}$. Although these limits for mixed layer deepening at early and late times have been noted extensively in the literature, not as much information seems to be available which details the transition between the two. It is clear from Crapper and Linden [23] that the thickness of the interface is proportional to $t^{1/2}$ at low Peclet numbers, which indicates that molecular diffusion is the dominant process in the growth of the mixed layer. However, in our case, the Peclet number is large ($Pe > 200$), with diffusion having a less prominent role. One explanation for this is the occurrence of internal wave motion during these transition times, as seen in Figs. 14–16. Although this argument is plausible, future research is needed to shed more light on its validity.

We believe that the documented appearance of long internal waves in the convection chamber are a manifestation of an interaction between penetrative convection and long internal waves, where 'long' is used to denote a horizontal scale which is large compared to the mixed-layer depth. As discussed in the Introduction, the primary coupling between these two fields arises through an intrinsic phase instability. The susceptibility of the coupled system to this type of phase instability is quite dependent on the boundary conditions, being most energetic in the presence of stress-free boundary conditions. The no-slip boundary conditions applicable in the present experiment inhibit the development of the phase instability, especially at early times when the mixed layer is shallow. At later times when the mixed layer deepens significantly, the inhibiting effect of these no-slip conditions weakens and the intrinsic coupling mechanism is manifest. It is our opinion that this coupling would be much more vigorous, even at earlier stages in the experiment, under conditions where the mixed-layer is adjacent to a stress-free boundary. Of course, verification of this conjecture at Rayleigh numbers approaching natural conditions awaits the 'appropriate' experiment, but the present results already point to the generation of long internal waves through an intrinisic coupling.

Acknowledgements

This work was supported in part by the Office of Naval Research under Grants N00014-95-1-0041 and N00014-92-J-1062. Additional support from the ARCS Foundation is gratefully acknowledged.

Appendix. Characteristics of long internal waves in the experimental cell

In order to be able to characterize unambiguously the internal wave field within the system, a forcing experiment was undertaken in which the initial frequency spectrum was narrow band. To do this a seiching experiment was performed. The measured temperature and velocity fields in this case allow some quantitative evaluation of the internal wave field. We focus particularly on the long-wave field present in the cell. The advantage of the seiche forcing is that the internal wave field is dominated by only a few of the lowest modes.

The forced experiment described here employed a basin-scale internal wave which was setup in the manner shown in Fig. 24. After the convection cell had been sealed and the water recirculators were initiated to form the stable stratification, the cell was tilted about the y-axis. The tilt angle used in the present study was 1.4°. The experiment was allowed to stratify with the cell at this fixed tilt angle. The system was allowed to achieve a stable stratification during the setup time which was typically about six hours. Since the fluid was initially at room temperature, this temperature could be used as the average of the stratification, thus the top temperature was set to be $+1/2\Delta T$ above room temperature, whereas the bottom temperature was set to $-1/2\Delta T$ below room temperature, where ΔT is the top-to-bottom temperature difference. In this manner, heat diffusion proceeded from both the top and bottom boundaries to establish a nearly constant temperature gradient.

After the stratification was properly defined, the experiment was started by disconnecting Bath 2 (the original bottom boundary temperature bath) and connecting Bath 3 to the recirculating channels. The heated water in Bath 3 recirculated through the bottom of the convection cell and initiated convective motion. The temperature of Bath 3 was set equal to the isotherm at a height of 80% of the cell depth. The tilted cell was then returned to its normal, horizontal position after a delay time, of 300 seconds. A basin-scale wave was produced as a result of returning the cell to the horizontal.

Computation of the internal wave modes is based on the linear internal wave eigenvalue problem

$$\frac{\mathrm{d}^2\Theta_n}{\mathrm{d}z^2} + \frac{1}{k^2}\left\{\frac{N^2(z,t)}{\omega_n^2(t)} - 1\right\}\Theta_n = 0, \quad n = 1, 2, \ldots, \tag{12}$$

$$\Theta_n(0;t) = \Theta_n(10.7\ \mathrm{cm};t) = 0.$$

$\Theta_n(z;t)$ is the modal amplitude for the fluctuating temperature field $T'(z,t)$ associated with the nth internal wave mode, k is the horizontal wave number, and $\omega_n(t)$ is the slowly-varying frequency (eigenvalue). As noted in the discussion at the beginning of Section 3.1, the Brunt-Väisälä profile $N(z,t)$ is quasi-steady, being based on the slowly-varying mean temperature profile $T(z,t)$. Therefore, the frequency $\omega_n(t)$ of a discrete wavelength fitting into the cell must vary in time as the mixed-layer depth slowly increases due to penetrative convection.

For our purposes, three different representations of $N(z,t)$ were employed. The first representation (Model I) utilizes the complete profile based on the measured distribution $T(z,t)$ across the entire depth of the cell. In this representation $N(z,t)$ has a decaying tail that extends a considerable distance into the mixed layer where convective motions are active. Now, one may argue that the tail of the B-V profile in a region where velocities associated with convective motion are considerably stronger than velocities associated with the internal wave field should be ignored insofar as the internal wave modal structure is concerned. That is, the computed internal wave field should be based on a clear separation of the base state into a mixed layer and a stably stratified layer. This argument leads to two idealizations of the measured B-V profile.

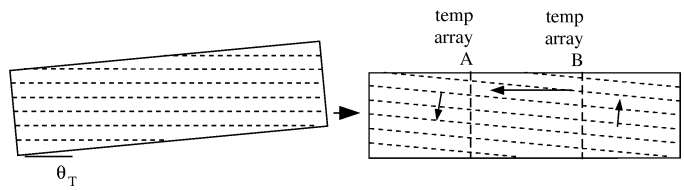

Fig. 24. Induced seiche wave schematic.

A first idealization of the B-V profile, called Model II, involves truncating the measured profile of $N(z,t)$ below some nominal interface level $z = h(t)$. The average interface height for this purpose was determined by locating the altitude at the intersection of the measured profile $N^2(z,t)$ with the value N^2_{avg}, where

$$N^2_{\text{avg}}(t) = \frac{1}{10.7}\int_0^{10.7} N(z,t)\,\mathrm{d}z. \tag{13}$$

The upper limit $z = 10.7$ cm was the altitude of the top surface of the convection cell. In this model, then, the measured profile $N(z,t)$ is used for 10.7 cm $> z > h(t)$ and $N = 0$ for $0 < z < h(t)$.

The second idealization of the B-V profile, called Model III, employs in Fig. 28 a simple two-layer approximation with a constant value $N(z,t) = N_0(t)$ for 10.7 cm $> z > h(t)$ and $N = 0$ for $0 < z < h(t)$, where $h(t)$ is determined as explained above. The value of $N_0(t)$ is chosen as the average value of $N(z,t)$ over the top few probe positions in the cell. These three different representations of the base-state B-V profile used for computing internal wave modes in this study are shown in Fig. 28.

The measured temperature fluctuations in the stratified part of the convection cell can be related to internal wave modes defined by (12) through the relation

$$T'(x,z,t) = \sum_{j=1}^{J} A_j \Theta_j(z,t)\sin\bigl[k_j(x-x_0) - \omega(t-t_0) + \phi_j\bigr]. \tag{14}$$

The reader will note that the time dependence in the temperature fluctuation is decomposed into a rapid oscillation with frequency ω and a slow variation of the orthonormal modal amplitude functions $\Theta_j(z,t)$. Of course, the frequency ω, amplitude A_j, and phase ϕ_j must also vary on the slow time scale as the mixed-layer thickness increases and the depth of the stratified layer diminishes. In writing this expression we also suppose that the frequency is given and consider k_j as the eigenvalue. This choice is dictated by the fact that specific peaks in the frequency spectra of T' could be unambiguously tracked directly from the data. The variation of the independent frequency peaks with time over the course of the forced experiment (Experiment B) is shown in Fig. 26. The frequency tracks in Fig. 26 were calculated, as described in the text, from moving, windowed FFTs of the fluctuating temperature signals in the stratified layer. The window used for the FFTs was 400 s.

It is evident that there is only one independent frequency track present in the first 1000 s of the seiche-forced experiment. This corresponds to the frequency of the seiche. Later in the experiment, after the seiche has essentially decayed, and after the thickness of the stably-stratified portion of the cell has diminished considerably, two new frequency tracks emerge at different times from the coupled dynamics of convection and internal waves (possibly through large-scale phase instabilities).

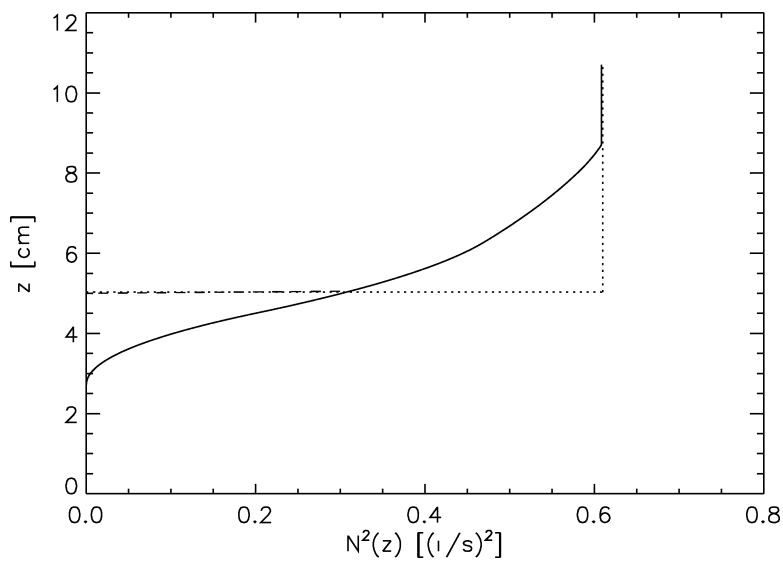

Fig. 25. Three system approximations for the N^2 profile: Model I - continuously stratified (—), Model II - modified two-layer (- - - -), Model III - simple two-layer (· · · ·).

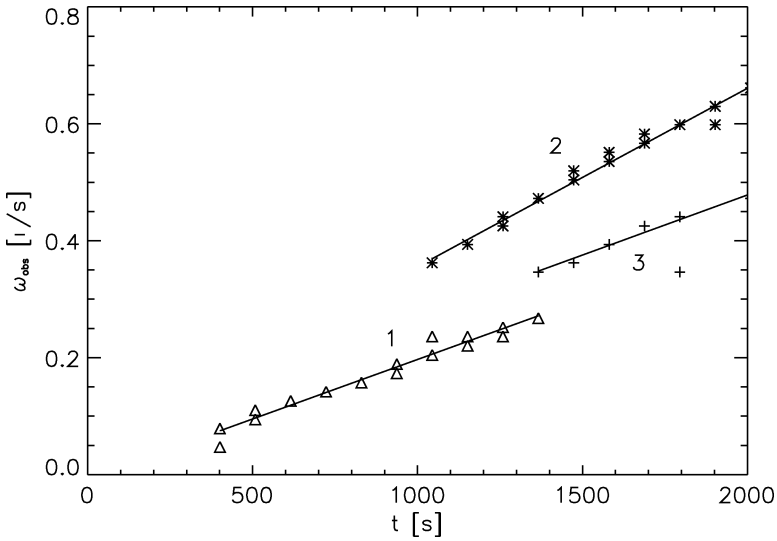

Fig. 26. Frequency variations with time ($N = 0.78\ \mathrm{s}^{-1}$). Legend: ($\triangle$) – frequency track 1 ($\partial\omega_1/\partial t = 0.00020$); ($*$) – frequency track 2 ($\partial\omega_2/\partial t = 0.00031$); ($+$) – frequency track 3 ($\partial\omega_3/\partial t = 0.00021$).

The slow temporal variation of the peak frequencies can be understood from the wave kinematic relations from Whitham [24]

$$\begin{aligned} &\frac{\partial\omega}{\partial t} + C_{\mathrm{g}}\frac{\partial\omega}{\partial x} = \frac{\partial\Omega}{\partial t}, \\ &\frac{\partial k}{\partial t} + C_{\mathrm{g}}\frac{\partial k}{\partial x} = -\frac{\partial\Omega}{\partial x}, \end{aligned} \tag{15}$$

where $C_g = \partial\omega/\partial k$ is the group velocity and $\omega = \Omega(k, x, t)$ is the dispersion relation for waves propagating in the inhomogeneous medium with slow space-time variations. We assume that the stratification is uniform in horizontal planes so $\partial\Omega/\partial x = 0$ and we can write $\mathrm{d}k/\mathrm{d}t = 0$ and

$$\frac{\mathrm{d}\omega}{\mathrm{d}t} = \frac{\partial\Omega}{\partial t} = \frac{\partial\Omega}{\partial h}\frac{\mathrm{d}h}{\mathrm{d}t}. \tag{16}$$

That is, the slow variation of the frequency is directly related to the depth of the mixed layer. Now, $\mathrm{d}h/\mathrm{d}t$ is known from the measured temperature structure and $\partial\Omega/\partial h$ can be computed from the internal wave eigenvalue problem (12) once a model for $N(z, t)$ is selected. Using the simple two-layer model of $N(z, t)$ with a variation of $\pm 10\%$ in the height of the 'interface' between the mixed layer and the stratified layer gave excellent agreement between measured values of $\mathrm{d}\omega/\mathrm{d}t$ and the right side of Eq. (16). Hence, it seems quite clear that the continuous increase in the frequency along the tracks shown in Fig. 26 is a consequence of the continuous diminution of the thickness of the stratified layer.

We use Eq. (14) and data measured by Array $\mathcal{A}$, which we assume is positioned at $x = x_0$, to construct a modal decomposition of the fluctuating temperature field. During the time interval of interest ($300\ \mathrm{s} < t < 600\ \mathrm{s}$), there are five temperature probes positioned in the stratified layer. Hence, we take $J = 5$ and write five equations of the form (14) using data at the five levels of the probes at a given time t. Next, we take the data at a later time $t + \Delta t$ from these same probes to obtain another set of five equations. Then, we select a particular model for $N(z, t)$ and compute the normalized eigenfunctions $\Theta_j(z, t)$ and the dispersion characteristics $k_j(\omega)$. After specifying the frequency, one can solve for the amplitude weights A_j and the phases ϕ_j for the five-mode representation of $T'(z, t)$. Since the base state varies slowly with time, however, this calculation must be repeated at later times following the path of the frequency track in Fig. 26 to evaluate the slow time variation of the eigenfunctions. One can also use the computed values of A_j and ϕ_j from the data at two times separated by a small interval Δt as described above to predict how the temperature fluctuation (and other physical quantities of interest) should vary over time scales small compared to ω^{-1}. Predictions of this sort can be used as a check on the validity of the modal decomposition.

We present first a calculation of the wavelengths $\lambda_j = 2\pi/k_j$ for the first five modes using Model II for the B-V profile. The calculations were performed for the observed frequency $\omega_{\mathrm{obs}} = 0.0862\ \mathrm{s}^{-1}$, and are shown in Table 3. Results are shown for an interface displaced upward and downward from the calculated position by 10% to exhibit the sensitivity in determining the wavelengths for the modes. The last column lists the wavelengths corresponding to different multiples of the cell length. It is seen that mode one corresponds closely with the lowest seiche mode for the cell, and that all other modes have wavelengths λ_i such that integral multiples of $\lambda_i/2$ are commensurate with the cell length.

Calculations of the wavenumbers k_j, eigenfunctions Θ_j, modal amplitudes A_j, and phases ϕ_j were made for the observed frequency along track 1 in Fig. 26 corresponding to a time centered around $t = 438$ s using all three models of the base state

Table 3
Comparing sensitivity of interface height in simplified two-layer approximation: dispersion relation values for Experiment B

	Interface height, $h - 10\%$	Interface height, h	Interface height, $h + 10\%$	Cell length multiples $L = 84.5$ cm
ω_{obs} [s^{-1}]	0.0862	0.0862	0.0862	
λ_1 [cm]	159.1	154.4	149.6	169.0: $L \sim \lambda_1/2$
λ_2 [cm]	67.4	64.7	61.8	63.4: $L \sim 3\lambda_2/2$
λ_3 [cm]	41.7	39.9	38.1	42.3: $L \sim 2\lambda_3$
λ_4 [cm]	30.1	28.8	27.4	28.2: $L \sim 3\lambda_4$
λ_5 [cm]	23.5	22.5	21.4	21.1: $L \sim 4\lambda_5$

Table 4
Comparing system approximations:vertical eigenfunction coefficients for forced seiche experiment (Experiment B), $\omega_{obs} = 0.0862$ s^{-1}

	Model I Continous stratification			Model II Simplified two-layer			Model III Modified two-layer		
Mode	k	Ampl.	Phase	k	Ampl.	Phase	k	Ampl.	Phase
1	0.043	0.017	2.23	0.041	0.012	2.25	0.045	0.013	2.25
2	0.098	0.011	–1.00	0.097	0.004	2.09	0.105	0.006	–1.00
3	0.155	0.010	2.21	0.157	0.005	2.29	0.169	0.006	2.30
4	0.212	0.004	–1.17	0.218	0.001	1.89	0.234	0.003	–1.03
5	0.269	0.001	1.70	0.230	0.000	1.35	0.300	0.001	1.96

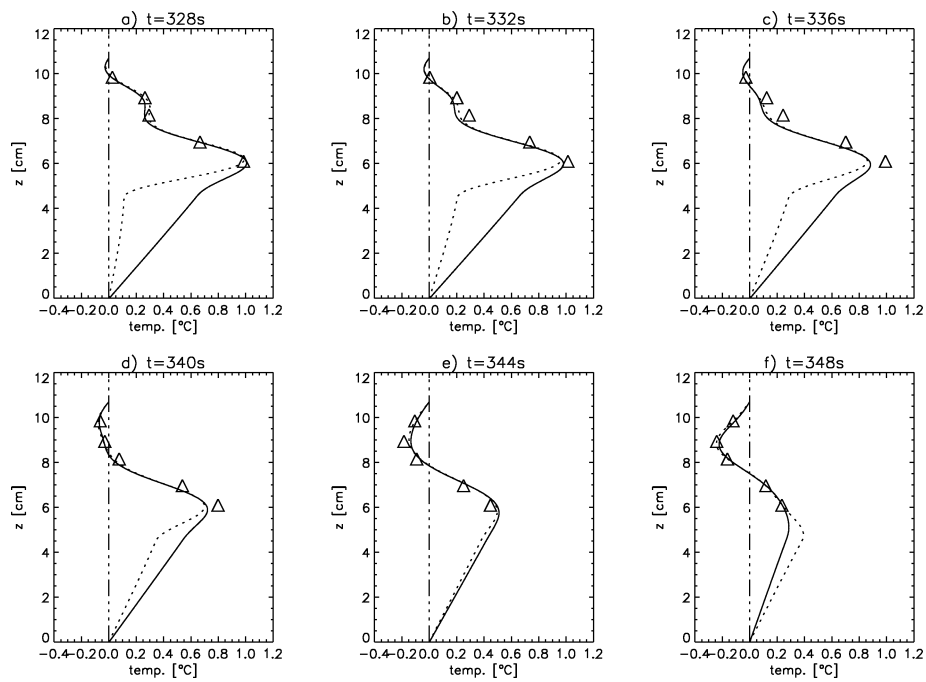

Fig. 27. Experiment B: Fluctuating temperature eigenfunction solutions. Legend: (· · · ·) – solution using simplified two-layer approximation (Model II); (——) – solution for modified two-layer approximation (Model III); △ – experimental fluctuating temperature data.

B-V profile. The modal parameters are given in Table 4. Peak frequencies were computed from a sliding window FFT applied to the experimental data. All the eigenfunctions have the maximums near the interface region. However, the eigenfunctions for the higher modes obtained using Model I are displaced markedly downward into the mixed layer relative to those using Models II and III.

Taking the information contained in Table 4, together with the associated eigenfunctions, a comparison can be made between the measured and the predicted temperature profiles for times outside the range of those used in constructing the modal decomposition. These comparisons are shown in Fig. 27. The modal representation using either Model II or III seems to track the structural changes in the measured data quite well, at least within this (admittedly rather narrow) time window. The time window for the predicted T' profile could be extended further, but temporal variations in the eigenfunctions $\Theta_j(z,t)$, amplitude weights $A_j(t)$, and phases $\phi_j(t)$ arising from the varying interface height $h(t)$ soon begin to degrade the quality of the prediction. Once a modal representation of the form (14) is in hand, one could proceed further and use the theory for linear internal waves to compute the velocity field corresponding to the wave-related temperature fluctuations.

The foregoing modal decomposition was applied at a time when the imposed seiche was prominent. It could, in principle, be continued to later times as the convective field penetrates deeper into the stratified layer. However, the number of temperature probes positioned within the stratified layer continually diminishes as $h(t)$ increases, limiting the number of modes that can be assessed through this decomposition procedure. Furthermore, as the penetrative process continues, the energy in the internal

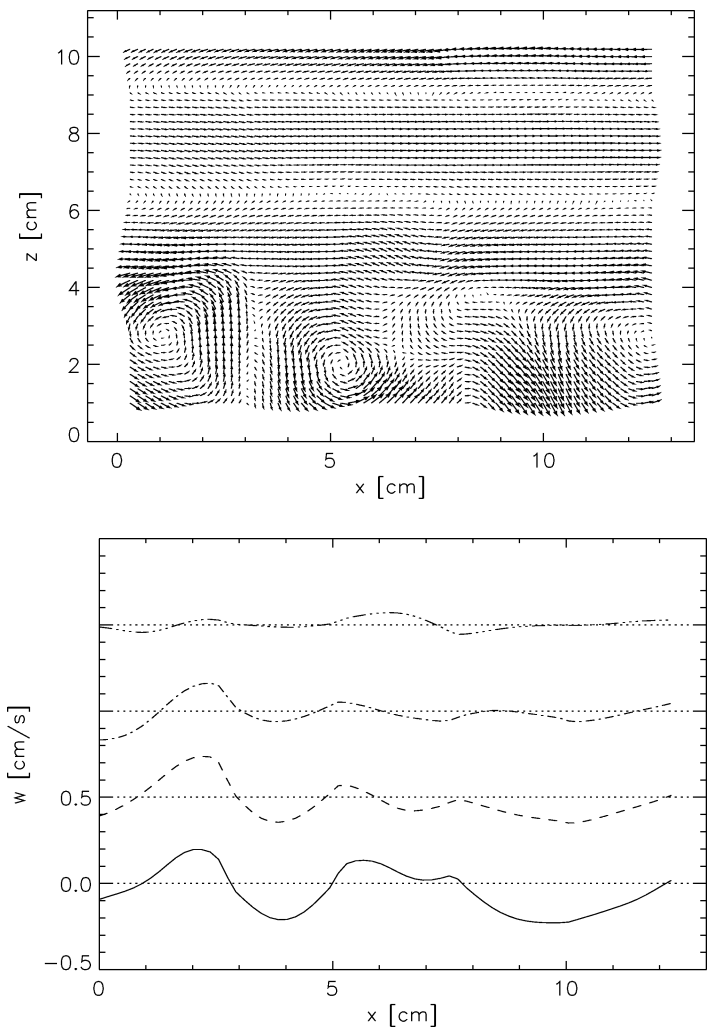

Fig. 28. Experiment B: seiche case, $N = 0.78\ \mathrm{s}^{-1}$. Top plot: Velocity vector plot of $x - z$ plane at $t = 355$ s. Lower plot: Vertical velocity profiles for different z locations at fixed time, $t = 355$ s. Legend: (——) – $z = 1$ cm; (– – –) – $z = 2$ cm; (– · –) – $z = 3$ cm; (– · · · –) – $z = 4$ cm.

wave field in this shallow, confined system is distributed more uniformly over a wider number of active modes. This clearly limits the usefulness of this decomposition technique to early times. In fact, the particular time window for calculation of the internal wave modes was partly predicated on the fact that the five probe levels were sufficiently deep in the stratified layer so that temperature perturbations forced by convective plumes could be assumed small in comparison to that associated with the wave field. This assumption is difficult to quantify. Nevertheless, and this is one of the particular advantages of the forced-wave experiment described here, the modal decomposition for early times when the spectral and modal content of the internal wave field is relatively simple reveals that, for example, the observed frequency tracks shown in Fig. 26 can be rationalized quite convincingly in terms of the slowly-varying nature of the internal wave guide. As a consequence, we propose that the emergence of two independent frequency tracks as the forced seiche decays is a manifestation of an intrinsic convection-internal wave coupling, albeit with a number of vertical modes encompassing a spectrum of discrete wavelengths that are rational multiples of the cell length.

As discussed in section 2.4, the velocity field in a vertical plane adjacent to temperature Array $\mathcal{A}$ was measured by means of the CIV technique. A realization of the measured velocity field during the seiche forcing at $t = 355$ s, 55 s following initiation of the seiche, is shown in the upper part of Fig. 28. Convective eddy motions are evident in the lower portion of the vector-field plot and the presence of a large-scale horizontal wave field is evident in the upper portion of the plot. The interfacial region shows evidence of weak short waves (see motion at location $x = 6$ cm, $z = 5$ cm). Vertical velocities at different levels in the convective region of the CIV window are shown in the lower part of the figure. An eddy with a lateral scale of about 4 cm is prominent near the left boundary of the CIV window. The interface between the lower convective layer and the upper, stably-stratified layer is roughly around the 5 cm level at the time of this velocity image.

References

[1] P. Coullet, P. Huerre, Resonance and phase solitons in spatially-forced thermal convection, Physica D 23 (1986) 27–44.
[2] A.J. Bernoff, Finite amplitude convection between stress-free boundaries: Ginzburg–Landau equations and modulation theory, Eur. J. Appl. Math. 5 (1994) 267–282.
[3] A.C. Newell, T. Passot, J. Lega, Order parameter equations for patterns, Annu. Rev. Fluid Mech. 25 (1993) 399–453.
[4] S. Pavithran, L.G. Redekopp, The coupling of gravity waves and convection: amplitude equations and planform selection, Stud. App. Math. 93 (1994) 209–250.
[5] A.C. Newell, J.A. Whitehead, Finite bandwidth, finite amplitude convection, J. Fluid Mech. 38 (2) (1996) 279–303.
[6] L.A. Segel, Distant sidewalls cause slow amplitude modulation of cellular convection, J. Fluid Mech. 38 (1969) 203–224.
[7] A.A. Townsend, Excitation of internal waves by a turbulent boundary layer, J. Fluid Mech. 22 (2) (1965) 241–252.
[8] A.A. Townsend, Internal waves produced by a convective layer, J. Fluid Mech. 24 (2) (1966) 307–319.
[9] J.W. Deardorff, G.E. Willis, D.K. Lilly, Laboratory investigation of non-steady penetrative convection, J. Fluid Mech. 35 (1) (1969) 7–31.
[10] J.S. Turner, The behaviour of a stable salinity gradient heated from below, J. Fluid Mech. 33 (1) (1968) 183–200.
[11] J.A. Whitehead, M.M. Chen, Thermal instability and convection of a thin fluid layer bounded by a stably stratified region, J. Fluid Mech. 40 (3) (1970) 549–576.
[12] T.I. McLaren, A.D. Pierce, Fohl T., B.L. Murphy, An investigation of internal gravity waves generated by a buoyantly rising fluid in a stratified medium, J. Fluid Mech. 57 (2) (1973) 229–240.
[13] J.W. Deardorff, G.E. Willis, B.H. Stockton, Laboratory studies of the entrainment zone of a convectively mixed layer, J. Fluid Mech. 100 (1980) 41–64.
[14] H.J.S. Fernando, R.-R. Chen, D.L. Boyer, Effects of rotation on convective turbulence, J. Fluid Mech. 228 (1991) 513–547.
[15] F.D. Heidt, The growth of the mixed layer in a stratified fluid due to penetrative convection, Bound.-Lay. Meteorol. 12 (1977) 439–461.
[16] M.E. Michaelian, The coupling between turbulent penetrative convection and internal waves, PhD thesis, University of Southern California, 1998.
[17] A.M. Fincham, G.R. Spedding, Low cost, high resolution DPIV for measurement of turbulent flow, Exp. Fluids 23 (1997) 449–462.
[18] P.F. Linden, The deepening of a mixed layer in a stratified fluid, J. Fluid Mech. 71 (2) (1975) 385–405.
[19] H. Kato, O.M. Phillips, On the penetration of a turbulent layer into stratified fluid, J. Fluid Mech. 37 (4) (1969) 643–655.
[20] P.P. Niiler, Deepening of the wind-mixed layer, J. Mar. Res. 33 (1975) 405–422.
[21] K.L. Denman, A time-dependent model of the upper ocean, J. Phys. Oceanogr. 3 (1973) 173–184.
[22] K.L. Denman, M. Miyake, Upper layer modification at ocean station papa: observations and simulation, J. Phys. Oceanogr. 3 (1973) 185–196.
[23] P.F. Crapper, P.F. Linden, The structure of turbulent density interfaces, J. Fluid Mech. 65 (1) (1974) 45–63.
[24] G.B. Whitham, Linear and Nonlinear Waves, Wiley, 1974.